

# Quantum crosstalk analysis for simultaneous gate operations on superconducting qubits

Peng Zhao,<sup>1,\*</sup> Kehuan Linghu,<sup>1,†</sup> Zhiyuan Li,<sup>1</sup> Peng Xu,<sup>2</sup> Ruixia Wang,<sup>1</sup> Guangming Xue,<sup>1,‡</sup> Yirong Jin,<sup>1</sup> and Haifeng Yu<sup>1</sup>

<sup>1</sup>*Beijing Academy of Quantum Information Sciences, Beijing 100193, China*

<sup>2</sup>*Institute of Quantum Information and Technology, Nanjing University of Posts and Telecommunications, Nanjing, Jiangsu 210003, China*

(Dated: February 9, 2022)

Maintaining or even improving gate performance with growing numbers of parallel controlled qubits is a vital requirement for fault-tolerant quantum computing. For superconducting quantum processors, though isolated one- or two-qubit gates have been demonstrated with high fidelity, implementing these gates in parallel commonly shows worse performance. Generally, this degradation is attributed to various crosstalks between qubits, such as quantum crosstalk due to residual inter-qubit coupling. An understanding of the exact nature of these crosstalks is critical to figuring out respective mitigation schemes and improved qubit architecture designs with low crosstalk. Here we give a theoretical analysis of quantum crosstalk impact on simultaneous gate operations in a qubit architecture, where fixed-frequency transmon qubits are coupled via a tunable bus, and sub-100-ns controlled-Z (CZ) gates can be realized by applying a baseband flux pulse on the bus. Our analysis shows that for microwave-driven single-qubit gates, the dressing from the qubit-qubit coupling can cause non-negligible cross-driving errors when qubits operate near frequency collision regions. During CZ gate operations, although unwanted nearest-neighbor interactions are nominally turned off, sub-MHz parasitic next-nearest-neighbor interactions involving spectator qubits can still exist, causing considerable leakage or control error when one operates qubit systems around these parasitic resonance points. To ensure high-fidelity simultaneous operations, there could raise a request to figure out a better way to balance the gate error from target qubit systems themselves and the error from non-participating spectator qubits. Overall, our analysis suggests that towards useful quantum processors, the qubit architecture should be examined carefully in the context of high-fidelity simultaneous gate operations in a scalable qubit lattice.

## I. INTRODUCTION

In pursuit of a useful quantum processor, the quality of qubits (e.g., qubit coherence time and fidelity of gate operations), and the number of qubits are two of the most important figures of merit. Nonetheless, in the practical implementation of quantum processors, an outstanding challenge is how to maintain or even improve gate performance with growing numbers of parallel controlled qubits [1]. For quantum processors built with superconducting qubits, isolated single-qubit gates with gate error below 0.1% [2–5] and two-qubit gates with gate error approaching 0.1% [2, 6–13] have been demonstrated in various qubit architectures [2]. However, in multi-qubit systems, implementing gate operations in parallel has commonly shown worse gate performance, especially for simultaneous two-qubit gate operations applied to nearby qubits, where gate errors are typically increased by 0.1%–1% [14–18]. Generally, the performance degradation is caused by the crosstalk effect [15, 19] that breaks the textbook assumption on quantum computing, i.e., gate operations are implemented spatially locally and independently (for a high-level and hardware-agnostic definition of crosstalk, we refer the reader to Ref. [19] for details). Moreover, this crosstalk effect can cause not just increased gate errors but even a variety of correlated and nonlocal errors which are particularly harmful to the realization of fault-tolerant quantum computing [20]. Thus, mitigating the crosstalk effect is critical to improving gate per-

formance in superconducting quantum processors and achieving the long-term goal of fault-tolerant quantum computing.

Recently, various studies on the detection, characterization, and mitigation of crosstalk have been published [8, 18, 19, 21–39]. From a high-level and hardware-agnostic perspective, several schemes have been proposed for detecting and characterizing crosstalk in multi-qubit systems [19, 21–26]. Meanwhile, by taking software strategies, various mitigation schemes have also been proposed, such as, at the qubit- or gate-level, one first characterizes the crosstalk and then actively cancels it with compensated pulses [8, 18, 27–33] or optimal control pulses [34–36], and at the quantum circuit level, one takes better crosstalk-aware compilation schemes and instruction scheduling schemes for implementing quantum algorithms [37–39]. However, these detection and characterization schemes cannot in general directly clarify the exact nature of crosstalk, and these software approaches for mitigating crosstalk commonly require complex control and characterization, thus placing heavy resource burdens on the control system and limiting their feasibility for large-scale quantum computing. Given these considerations, besides taking high-level software strategies, it is highly desirable to further understand crosstalk and figure out how to mitigate crosstalk from a hardware perspective.

Crosstalk that appears in multi-qubit superconducting quantum processors is commonly very architecture-dependent. For example, in qubit architectures with fixed coupling and fixed-frequency qubits [14], the dominated crosstalk is associated with microwave crosstalk and residual inter-qubit coupling [10, 11, 21], whereas in qubit architectures with frequency-tunable qubits or tunable coupling [27, 40, 41], the flux crosstalk is considered as more involved [27, 28]. Despite its architecture-dependent multifariousness,

\*Electronic address: [shangniguo@sina.com](mailto:shangniguo@sina.com)

†Electronic address: [linghukh@baqis.ac.cn](mailto:linghukh@baqis.ac.cn)

‡Electronic address: [xuegm@baqis.ac.cn](mailto:xuegm@baqis.ac.cn)

from the hardware perspective, crosstalk can be categorized into two types according to its physical origination [42]. One is the classical crosstalk associated with unintended classical electromagnetic couplings, such as DC or AC flux crosstalk [28, 29] and microwave crosstalk [8, 10, 11]. The other one is quantum crosstalk resulting from inter-qubit couplings, such as residual nearest-neighbor (N.N.) coupling [11, 27] and next-nearest-neighbor (N.N.N.) coupling [27, 41, 43]. An understanding of the exact nature of crosstalk or separating error contributions from different crosstalks is an urgent need for figuring out respective mitigation schemes and for obtaining improved qubit architecture designs with low crosstalk. Although several works have previously examined various quantum crosstalk effects, such as  $ZZ$  crosstalk for single-qubit gates [21, 44, 54], two-qubit gates [10, 11, 33, 44–54], and spectator-qubit induced crosstalk in multi-qubit systems [30–33, 55–57], they are restricted mainly to isolated two-qubit gates. Crosstalk analysis in the context of simultaneous gate operations on a multi-qubit lattice could provide more physical insight into the nature of the crosstalk effect [18, 58] on practically implemented quantum processors [15, 16].

In this work, we give a theoretical analysis of quantum crosstalk impact on simultaneous gate operations in a qubit architecture with tunable  $ZZ$  coupling, as sketched in Fig. 1, where fixed-frequency transmon qubits [59] are coupled via a tunable bus [60]. To do so, we first give detailed descriptions of the proposed qubit architecture, especially focusing on the tunable  $ZZ$  coupling enabled by the tunable bus, gate operations, and the scalability of the architecture. We then turn to illustrate the quantum crosstalk effect on simultaneous gate operations in this qubit architecture. We consider two typical gate operations, i.e., single-qubit X gate and two-qubit CZ gate:

(i) For simultaneous single-qubit X gate operations, the dressing from the qubit-qubit coupling can induce substantial quantum crosstalk, i.e., cross-driving effect, and the associated crosstalk strength is comparable with that of classical microwave (see Fig. 4). Focusing on the nearest-neighbor qubit pairs, we show that when qubit systems approach the frequency-collision region, the cross-driving effect can make gate performance worse by almost an order of magnitude (see Fig. 6). This suggests that to ensure high-fidelity single-qubit addressing, this dressing-induced cross-driving effect should be considered as a serious contender of the error sources.

(ii) For simultaneous CZ gate operations, we show that due to the quantum crosstalk, the performance of simultaneous CZ gate operations can be almost an order of magnitude worse than that of the isolated case (see Fig. 8). We further illustrate the exact nature of these quantum crosstalks, i.e., residual N.N.N. interactions with small coupling strength, and argue that although unwanted N.N. interactions are nominally turned off, sub-MHz parasitic N.N.N. interactions involving spectator qubits (enabled by high-order processes) can still exist. To mitigate their impact on simultaneous two-qubit gate operations, we show that engineering system parameters (e.g., pushing these parasitic N.N.N. interaction points away from the system working point) (see Fig. 10) or implementing short-time gate operations (see Fig. 12) could miti-

gate the quantum crosstalk impact on simultaneous gate operations. However, on the contrary, gate operations with a slower speed can, in general, suppress unwanted interactions within target qubit systems. Hence, we argue that for high-fidelity simultaneous gate operations, this could give rise to a trade-off between the error resulting from target qubit systems themselves and the error from non-participating spectator qubits (see Fig. 12). More strikingly, this trade-off suggests that even without the consideration of qubit decoherence error, gate operations with slower speeds do not always show better performance.

Overall, the analysis presented in this work shows that isolated gate performance, especially, obtained with all non-participating spectator qubits in their ground states, cannot capture its true performance for the realistic situation in which gates are implemented simultaneously. Towards a functional quantum processor, the performance of quantum processors should be examined carefully in the context of simultaneous gate operations. The analysis can improve our understanding of the exact nature of quantum crosstalk and its impact on simultaneous gate operations, thus may also pave the way for figuring out crosstalk mitigation schemes and qubit architecture designs with low crosstalk. Additionally, the result of this analysis also suggests that the proposed qubit architecture may be a promising architecture towards a large-scale superconducting quantum processor with low crosstalk.

This paper is organized as follows. In Sec. II, we introduce our qubit architecture and give a detailed description of the gate operation in this qubit architecture. In Sec. III, we numerically study the performance of simultaneous gate operations (i.e., simultaneous single-qubit and two-qubit gate operations) in the qubit architecture introduced in Sec. II, analyze the leading error source (i.e., quantum crosstalk) of the added error for the parallel implemented gate operations, and show how to mitigate quantum crosstalk impact on gate operations. In Sec. IV, we give conclusions of our investigation.

## II. FIXED-FREQUENCY QUBIT ARCHITECTURES WITH TUNABLE BUSES

In this section, we propose a qubit architecture comprising fixed-frequency transmon qubits coupled via a tunable bus, as shown in Fig. 1(b). We first focus specifically on this single building block and show how qubit-bus coupling can enable a high-contrast  $ZZ$  interaction. Therefore, high fidelity single-qubit gates can be achieved with suppression of  $ZZ$  crosstalk, and a sub-100-ns CZ gate can be realized when we switch on the  $ZZ$  interaction between qubits. Then, we consider scaling up this building block to scalable two-dimensional (2D) qubit grids.

### A. System Hamiltonian and tunable $ZZ$ coupling

Here, we consider a system of two transmon qubits depicted in Fig. 1(b), where two transmon qubits  $Q_{1,2}$  are coupled through a tunable bus  $TB$  (a third ancilla frequency-

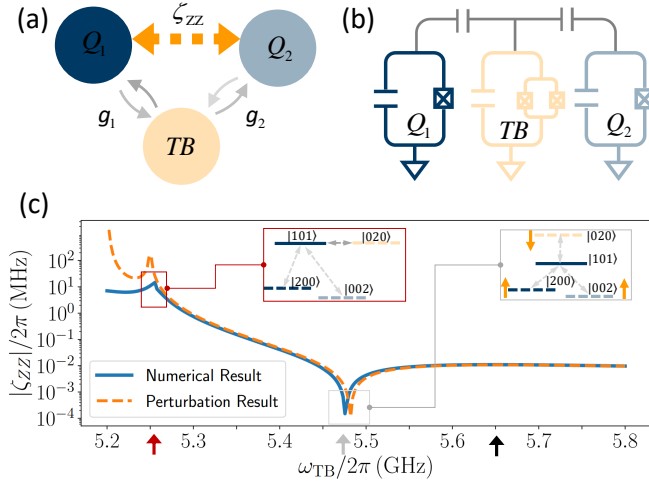


FIG. 1: (a) Sketch of a coupled two-qubit system ( $Q_{1,2}$ ) with tunable ZZ interaction  $\zeta_{ZZ}$  enabled by the tunable bus (TB). (b) Circuit diagram of two fixed-frequency transmons coupled via a frequency-tunable transmon (treated as a tunable bus). (c) ZZ coupling  $\zeta_{ZZ}$  as a function of bus frequency  $\omega_{TB}$  for the qubit system illustrated in (b) with qubit frequency  $\omega_{1(2)}/2\pi = 5.000(5.200)$  GHz, anharmonicity  $\eta_1 = \eta_2 = \eta_{TB} = \eta$  ( $\eta/2\pi = -300$  MHz), and qubit-bus coupling  $g_{1(2)} = g$  ( $g/2\pi = 25$  MHz) (at  $\omega_{1(2)} = \omega_{TB} = 5.500$  GHz). The blue-solid and orange-dashed lines represent the numerical and perturbational results, respectively. The red arrow indicates the working point where a strong ZZ coupling exists due to the resonance interaction  $|101\rangle \leftrightarrow |020\rangle$  (as shown in the inset outlined with red line), and grey arrow shows the ZZ-free point resulting from the destructive interference of ZZ contributions from interactions  $|101\rangle \leftrightarrow \{|200\rangle, |002\rangle, |020\rangle\}$  (as shown in the inset outlined with grey line). To ensure high-fidelity single-qubit addressing, besides the residual ZZ crosstalk, the cross-driving crosstalk due to qubit state dressing should also be taken into consideration (see Sec. II B for details). In light of this, the system idle point is typically 500 MHz above the qubit in frequency, marked by the black arrow.

tunable transmon qubit). The full system can be modeled by a chain of three weakly anharmonic oscillators [59] with nearest-neighboring coupling, and can be described by (hereafter  $\hbar = 1$ , notation  $|Q_1 TB Q_2\rangle$  represents states of the full system, and when restricted to the qubit-subspace, notation  $|Q_1 Q_2\rangle$  is used),

$$H = \sum_l \left[ \omega_l a_l^\dagger a_l + \frac{\eta_l}{2} a_l^\dagger a_l^\dagger a_l a_l \right] + \sum_n \left[ g_n (a_n^\dagger a_{TB} + a_n a_{TB}^\dagger) \right], \quad (1)$$

where the subscript  $l \in \{1, 2, TB\}$  labels  $l$ th oscillator  $\{Q_1 Q_2 TB\}$  with anharmonicity  $\eta_l$  and frequency  $\omega_l$ ,  $a_l$  ( $a_l^\dagger$ ) is the associated annihilation (creation) operator, and  $g_n$  ( $n = 1, 2$ ) denotes the strength of the coupling between qubit  $Q_n$  and the tunable bus. The qubit-bus coupling can mediate an effective ZZ coupling between qubits, which is defined as

$$\zeta_{ZZ} \equiv (E_{11} - E_{10}) - (E_{01} - E_{00}) \quad (2)$$

where  $E_{jk}$  denotes eigenenergy of system associated with dressed eigenstate  $|j\bar{k}\rangle$ , which is adiabatically connected to the bare state  $|j0k\rangle$ . According to the fourth-order perturbation theory [61], this effective ZZ coupling can be approximated as [44, 46, 62]

$$\zeta_{ZZ} = 2g_1^2 g_2^2 \left[ \frac{1}{\Delta_2^2 (\Delta - \eta_1)} - \frac{1}{\Delta_1^2 (\Delta + \eta_2)} \right] + \frac{2g_1^2 g_2^2}{\Delta_1 + \Delta_2 - \eta_{TB}} \left[ \frac{1}{\Delta_1} + \frac{1}{\Delta_2} \right]^2, \quad (3)$$

where  $\Delta_{1(2)} = \omega_{1(2)} - \omega_{TB}$ , and  $\Delta = \omega_2 - \omega_1$  denote the qubit-bus detuning and qubit-qubit detuning, respectively. In the above expression for ZZ coupling strength, the first two terms result from the interaction  $|101\rangle \leftrightarrow \{|200\rangle, |002\rangle\}$ , and the final one contributes from interaction  $|101\rangle \leftrightarrow |020\rangle$  [49, 63].

We first consider how to suppress ZZ coupling at the system idle point, where single-qubit gates can be implemented with suppression of ZZ crosstalk. From Eq. (3), one can find that ZZ-free point, i.e.,  $\zeta_{ZZ} = 0$ , is independent of the qubit-bus coupling strengths. Assuming  $\eta_1 = \eta_2 = \eta_{TB} = \eta$  and considering  $\omega_1 \simeq \omega_2$ , the ZZ-free point is at  $\Delta_{1(2)} \simeq 3\eta/2$ , where the qubit-bus detuning has a magnitude similar to that of qubit anharmonicity [64]. For transmon qubits with a typical anharmonicity of 300 MHz and operated in the dispersive regime (i.e.,  $|\Delta_{1(2)}| \geq 10g_{1(2)}$ ), this means that to suppress residual ZZ interaction, the qubit-bus coupling strength should take a value far less than that of the conventional qubit-bus coupling, the strength of which is typically 100 MHz [60, 63]. Note here that although qubit systems can in principle operate in the non-dispersive regime (i.e.,  $|\Delta_{1(2)}| \ll 10g_{1(2)}$ ), single qubit addressing and eliminating unwanted parasitic interactions, such as N.N.N. coupling, may become highly nontrivial [64].

Thus, below, we consider that the qubit-bus coupling strength takes the value  $g_{1(2)}/2\pi = g/2\pi = 25$  MHz, which is similar to the qubit-qubit coupling strength in the conventional qubit architecture with fixed direct coupling [27]. In this way, at the idle point, where the qubit system operates in the dispersive regime, both the qubit addressing error and unwanted parasitic interaction could be suppressed heavily. However, one may doubt that how this rather small qubit-bus coupling can enable a bus-mediated inter-qubit interaction with adequate strength for implementing a successful two-qubit gate. Figure 1(c) shows the ZZ coupling strength versus bus frequency with qubit frequency  $\omega_{1(2)}/2\pi = 5.000(5.200)$  GHz, anharmonicity  $\eta_1 = \eta_2 = \eta_{TB} = \eta$  ( $\eta/2\pi = -300$  MHz). The observation is that the destructive interference of ZZ coupling contributions from interactions  $|101\rangle \leftrightarrow \{|200\rangle, |002\rangle, |020\rangle\}$  (see Fig. 1(c), the inset outlined with red line) gives rise to a ZZ-free point at frequency  $\omega_{TB}/2\pi = 5.475$  GHz, where the qubit-bus detuning is comparable to the qubit anharmonicity. This confirms the perturbational analysis given above. When biasing the bus at frequency  $\omega_{TB}/2\pi \simeq 5.250$  GHz, there exists a ZZ coupling with a strength of 10 MHz, which is adequate and suitable for implementing a sub-100-ns CZ gate.

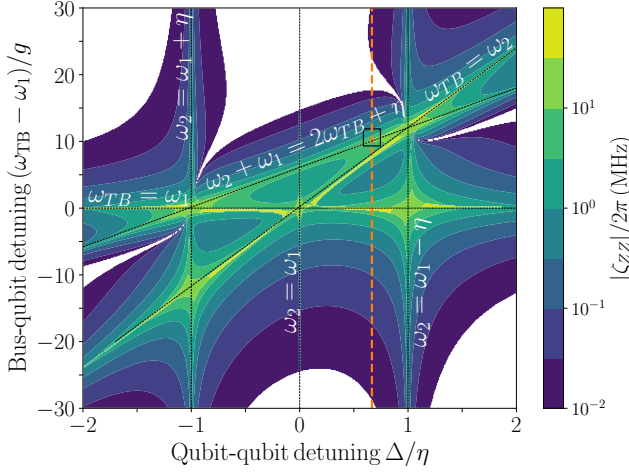


FIG. 2:  $ZZ$  coupling  $\zeta_{ZZ}$  (data points with  $ZZ$  coupling strengths below 10 kHz are removed) as a function of qubit-qubit detuning and bus-qubit detuning, where the frequency of  $Q_2$  is fixed at  $\omega_1/2\pi = 5.000$  GHz. Other system parameters are the same as those used in Fig. 1(c). Vertical cut (orange dashed line) denotes the result plotted in Fig. 1(c), and open black square marks the working point at  $\omega_{\text{on}} = \bar{\omega} - \eta_{\text{TB}}/2$  with the mean qubit frequency  $\bar{\omega} = (\omega_1 + \omega_2)/2$ .

This  $ZZ$  interaction mainly results from the resonance interaction  $|101\rangle \leftrightarrow |020\rangle$  (see Fig. 1(c), the inset outlined with grey line) at the working point  $\omega_{\text{on}} = \bar{\omega} - \eta_{\text{TB}}/2$ , where  $\bar{\omega} = (\omega_1 + \omega_2)/2$  denotes the mean qubit frequency.

In addition, by fixing  $Q_1$ 's frequency at 5.000 GHz, Figure 2 shows the  $ZZ$  coupling strength  $\zeta_{ZZ}$  (data points with  $ZZ$  coupling strengths below 10 kHz are removed) as a function of qubit-qubit detuning  $\Delta$  and bus-qubit detuning. One can find that suppression of  $ZZ$  coupling can be achieved in several parameter zones, such as the straddling regime (i.e., qubit-qubit detuning  $|\Delta_{1(2)}| < |\eta_{1(2)}|$ ) [44, 64], and out of the straddling regime with one qubit above and one qubit below the bus in frequency. Moreover, contrary to the conventional qubit-bus system [44], one can find that for systems operated out of the straddling regime with qubits below or above the bus in frequency,  $ZZ$  interaction can still be heavily suppressed. This is to be expected, because in the present qubit system, the qubit-bus coupling is far smaller than that of the conventional case.

## B. Gate operation

The above illustration shows that the proposed qubit architecture is promising to achieve high-contrast  $ZZ$  interactions in several different parameter regions. Such flexibility in the choice of parameters can potentially be used to explore various possible advantages for implementing a scalable quantum processor. In the following discussion, we focus specifically on the straddling regime, i.e.,  $|\Delta| < |\eta|$ .

Two-qubit unit cell	Collision conditions	Unwanted transitions
	(1). $\omega_i = \omega_j$	$ 0\rangle_j \rightarrow  1\rangle_j$
	(2). $\omega_i = \omega_j + \eta_j/2$	$ 0\rangle_j \rightarrow  2\rangle_j$
	(3). $\omega_i = \omega_j + \eta_j$	$ 1\rangle_j \rightarrow  2\rangle_j$

FIG. 3: Qubit frequency collision conditions and their associated unwanted transitions.

### 1. single-qubit gate

As usual, the  $ZZ$ -free point is chosen as the system idle point, thus single-qubit gates can be implemented without the detrimental effect from residual  $ZZ$  interaction. However, we note that for microwave-activated single-qubit gates, while residual  $ZZ$  coupling is eliminated, there can exist another error source, i.e., cross-driving error. The cross-driving error describes a phenomenon that microwave driving applied to one qubit can cause unintended driving on the others [21, 42]. This can be due to classical microwave crosstalk or qubit state dressing (resulting from inter-qubit coupling) induced quantum crosstalk. Here, we restrict ourselves to the last case. Unlike the cross-driving effect resulting from classical microwave crosstalk, the qubit-dressing induced one can create a non-local coherent error on coupled qubits. The exact nature of this cross-driving effect is essentially the same as the cross-resonance (CR) interaction [21, 65, 66], and CR interaction can be seen as a special cross-driving effect, where one intends to maximize the "non-local coherent error", thereby, enabling the implementation of a two-qubit gate, i.e., CR gate.

Similar to the classical microwave crosstalk, when we focus on an individual qubit, the dressing-induced cross-driving can excite qubits, causing unintended single-qubit rotation or leakage out of the qubit-subspace. This can result in a substantially large gate error, especially when considering the qubit system operated near the frequency collision regions [56, 68]. As shown in Fig. 3, there are three main types of frequency collisions: (Type-1) when the frequencies of two coupled qubits are close to the on-resonance condition, the cross-driving between qubits can cause transition within computational subspace, leading to unintended single-qubit rotations; when one qubit's frequency is nearly on-resonance with the frequency of two-photon transition  $|0\rangle \leftrightarrow |2\rangle$  (Type-2) or high-level transitions  $|1\rangle \leftrightarrow |2\rangle$  (Type-3) of others, the cross-driving can result in population leakage out of qubit-subspace.

For illustration purposes, here we consider a microwave driving with a constant amplitude applied to  $Q_1$  in the two-qubit system described by Hamiltonian in Eq. (1), intending to implement a single-qubit gate on  $Q_1$ . The driven Hamiltonian can be described by

$$H_d = [\Omega_x(t) \cos(\omega_d t) + \Omega_y(t) \sin(\omega_d t)](a_1^\dagger + a_1), \quad (4)$$

with  $\Omega_d(t) \equiv \Omega_x(t) + i\Omega_y(t)$ , where  $\Omega_d(t) = \Omega$  denotes the



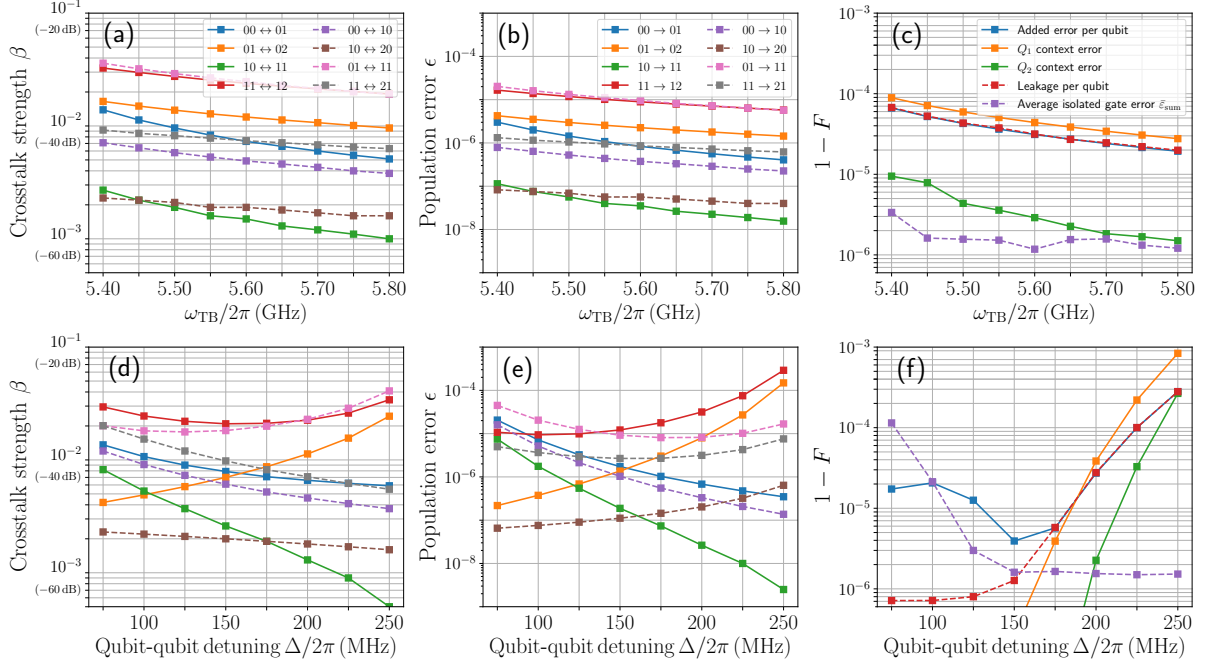


FIG. 4: (a-c) Dressing induced cross-driving effect between coupled qubits  $Q_{1(2)}$  versus bus frequency with other system parameters same as those used in Fig. 1. (d-f) Cross-driving effect versus qubit-qubit detuning  $\Delta$  with bus frequency  $\omega_{\text{TB}}/2\pi = 5.650$  GHz and qubit frequency  $\omega_1/2\pi = 5.000$  GHz. Other system parameters are the same as in Fig. 1. For coupled qubits  $Q_{1(2)}$ , when a microwave driving with strength  $\Omega$  is applied to one qubit, the nearby qubit can also be felt by driving with amplitude  $\tilde{\Omega}$  (i.e., cross-driving), which is dependent on qubit states. (a) and (d) show the crosstalk strength between coupled qubits, defined as  $\beta \equiv \tilde{\Omega}/\Omega$ . Here,  $0j \leftrightarrow 0k$  and  $1j \leftrightarrow 1k$  label the cross-driving applied on the transition  $|j\rangle \leftrightarrow |k\rangle$  of  $Q_2$  with  $Q_1$  in its ground state and excited state, respectively. Similarly,  $j0 \leftrightarrow k0$  and  $j1 \leftrightarrow k1$  label the cross-driving applied on the transition  $|j\rangle \leftrightarrow |k\rangle$  of  $Q_1$  with  $Q_2$  in its ground state and excited state, respectively. (b) and (e) show the worst-case population error caused by cross-driving. Here,  $0j \rightarrow 0k$  ( $1j \rightarrow 1k$ ) labels the worst case population on  $|k\rangle$  of  $Q_2$ , where  $Q_2$  is prepared in state  $|j\rangle$  and the  $Q_1$  is in its ground state (excited state). (c) and (f) present the single-qubit gate error ( $1 - F$ ) under the influence of the cross-driving effect between qubits.

driving amplitude, and  $\omega_d$  is the driving frequency. Similar to the CR interaction, the cross-driving from  $Q_1$  to  $Q_2$  is dependent on the state of  $Q_1$ . By diagonalizing the undriven system Hamiltonian (at the idle point) in Eq. (1), one can obtain the dressed eigenstate  $|j\tilde{k}\rangle$ . Then, rewriting the driven Hamiltonian Eq. (3) in terms of the dressed eigenstate, one can obtain strength of the cross-driving from  $Q_1$  to  $Q_2$  (similar analysis can also be applied to the cross-driving from  $Q_2$  to  $Q_1$ ). For example, the strength of the cross-driving from  $Q_1$  to  $Q_2$  can be approximated as

$$\begin{aligned}\tilde{\Omega}_{00 \leftrightarrow 01} &\simeq \frac{J\Omega}{\Delta}, \\ \tilde{\Omega}_{10 \leftrightarrow 11} &\simeq \frac{J\Omega(\Delta + \eta_1)}{\Delta(\Delta - \eta_1)}, \\ \tilde{\Omega}_{01 \leftrightarrow 02} &\simeq \frac{\sqrt{2}J\Omega}{\Delta + \eta_2}, \\ \tilde{\Omega}_{11 \leftrightarrow 12} &\simeq \frac{\sqrt{2}J\Omega(\Delta + \eta_1 + \eta_2)}{(\Delta - \eta_1 + \eta_2)(\Delta + \eta_2)},\end{aligned}\quad (5)$$

where  $\tilde{\Omega}_{0j \leftrightarrow 0k}$  and  $\tilde{\Omega}_{1j \leftrightarrow 1k}$  denote the cross-driving applied to  $Q_2$ 's transitions  $|j\rangle \leftrightarrow |k\rangle$  for  $Q_1$  in the ground and ex-

cited states, respectively[67], and  $J$  denotes the effective bus-mediated exchange coupling, which can be approximated as  $J = (g_1 g_2 / 2)(1/\Delta_1 + 1/\Delta_2)$ .

Similar to the characterization of classical microwave crosstalk, we can define the crosstalk strength of this dressing-induced cross-driving as  $\beta \equiv \tilde{\Omega}/\Omega$ . Moreover, to quantify the cross-driving induced gate error, here we also introduce the worst-case population error (since off-resonance driving can cause incomplete Rabi oscillation, here we choose the maximum population amplitude as an indicator of the gate error and set  $\Omega/2\pi = 25$  MHz) defined as

$$\epsilon \equiv \frac{\tilde{\Omega}^2}{\tilde{\Omega}^2 + \delta^2}, \quad (6)$$

where  $\delta$  denotes the detuning between the cross-driving frequency and qubit's transition frequencies between different energy levels.

To ensure high-fidelity single-qubit gates, the cross-driving effect should be minimized. From the expression given in Eq. (5), this can be achieved by reducing exchange coupling  $J$  and avoiding the qubit frequency collisions shown in Fig. 3. Figures 4(a) and 4(b) show the crosstalk strength  $\beta$  between

$Q_1$  and  $Q_2$ , and the cross-driving induced population error versus bus frequency. One can find that both the crosstalk strength and the population error are indeed decreased as we increase the bus frequency. In Figs. 4(d) and 4(e), we also show the crosstalk strength and the population error versus qubit-qubit detuning  $\Delta$ . We find that the crosstalk strength itself is dependent on the detuning  $\Delta$ , and it is also highly asymmetric (also see Fig. 4(a)). For example, for qubits with lower frequency, i.e.,  $Q_1$ , the cross-driving from  $Q_2$  (with a higher qubit frequency) to  $Q_1$  becomes notable when  $Q_2$  is in the excited state (e.g.,  $|01\rangle \leftrightarrow |11\rangle$ ). Meanwhile, the crosstalk from  $Q_1$  to  $Q_2$  especially tends to give leakage out of qubit subspace (e.g.,  $|11\rangle \leftrightarrow |12\rangle$  and  $|01\rangle \leftrightarrow |02\rangle$ ). Nevertheless, as shown in Fig. 4(e), on the whole, the cross-driving impact on gate fidelity can still be captured by the frequency collision analysis:

(i) For coupled qubits with small qubit-qubit detuning, the system approaches Type-1 frequency collision, thus the dominated error from cross-driving is unintended single-qubit rotations, whereas the leakage error is suppressed.

(ii) When qubit-qubit detuning approaches the anharmonicity of qubits, i.e., the Type-3 frequency collision, the cross-driving induced leakage error is dominated and unintended rotation is greatly reduced. This suggests a fundamental trade-off between control error and leakage error.

(iii) The Type-2 frequency collision seems to have less impact on gate performance [69]. This is reasonable since the Type-2 frequency collision involves a second-order process that tends to be orders of magnitude weaker than that of Type-1 and Type-3.

In the discussion given above, the population error is just a rough estimation of the cross-driving induced gate error [70]. In practical implementations of single-qubit gates, rather than using a constant magnitude driving, one commonly uses a shaped pulse, e.g., Derivative Removal by Adiabatic Gate (DRAG) pulse [3, 4, 71], thus suppressing leakage out of qubit-subspace. In the following discussion, to implement a single qubit  $X$  gate, we consider using DRAG scheme with a 20-ns cosine-shaped pulse [3], given as  $\Omega_{\text{DRAG}}(t) = \Omega_x(t) - i\alpha\dot{\Omega}_x(t)/\eta$ , where  $\Omega_x(t) = A[1 - \cos(2\pi t/t_g)]/2$ ,  $t_g$  is the gate time,  $A$  is the peak pulse amplitude (for  $t_g = 20$  ns,  $A/2\pi \simeq 50$  MHz),  $\alpha$  is a free parameter that is chosen to suppress leakage error (see Appendix A 1 for details on the calibration procedure of  $X$  gates) [3, 4, 71].

To give a more exact characterization of the cross-driving impact on single-qubit gates, we consider the following virtual experiment: (1) First, an isolated single-qubit gate on qubit  $Q_{1(2)}$  is tuned up and characterized with the other qubit in its ground state, giving rise to the isolated gate fidelity, i.e.,  $F_{\blacksquare 0}$  (here the subscript denotes the state bitstring  $|\blacksquare 0\rangle$ , and for the active target system to which a gate operation is applied, its qubit state is labeled by  $\blacksquare$ ) for  $Q_1$  and  $F_{0\blacksquare}$  for  $Q_2$ . (2) Then, the same gate is re-characterized with the other qubit in its excited state, giving rise to  $F_{\blacksquare 1}$  for  $Q_1$  and  $F_{1\blacksquare}$  for  $Q_2$ . (3) Finally, we consider that both gates are implemented simultaneously, characterization of this composite gate, i.e.,  $X \otimes X$ , gives rise to the gate fidelity  $F_{X \otimes X}$ . Here, we define  $Q_1$  ( $Q_2$ ) context error  $|F_{\blacksquare 0} - F_{\blacksquare 1}|$  ( $|F_{0\blacksquare} - F_{1\blacksquare}|$ ) to characterize the

cross-driving impact on isolated single-qubit gates, and define added error per qubit  $(F_{\blacksquare 0}F_{0\blacksquare} - F_{X \otimes X})/2$  for simultaneous single-qubit gate operations.

To quantify the effect of cross-driving on the gate performance, we use the metric of gate fidelity given as (without qubit decoherence) [72]

$$F = \frac{\text{Tr}(\tilde{U}^\dagger \tilde{U}) + |\text{Tr}(U^\dagger \tilde{U})|^2}{d(d+1)}, \quad (7)$$

where  $U$  and  $\tilde{U}$  denote the target gate operation and implemented gate operation, respectively, and  $d$  represents the system dimension. In Figs. 4(c) and 4(f), we show the fidelity of  $X$  gate as a function of bus frequency and qubit-qubit detuning, respectively. Similar to the result shown in Figs. 4(b) and 4(e), one can find that reducing exchange coupling  $J$  indeed suppresses the cross-driving effect on single-qubit gates, and a non-negligible gate error of about 0.002%–0.1% (given the state-of-the-art single-qubit gate error approaching 0.01% [3, 4]) appears when the qubit-qubit detuning approaching Type-1 or Type-3 frequency collision region. To identify the nature of the added error, we also show the added leakage error per qubit [73]. As shown in Fig. 4(f), for qubit-qubit detuning near the Type-3 frequency collision, the leakage error is indeed the dominated error source, accounting for the added error during simultaneous gate operations. Moreover, the context error also coincides with the leakage, this is true since leakage out of qubit-subspace can only occur when the cross-driven qubit is in the excited state. On the contrary, the context error and leakage errors are far less important near the Type-1 frequency collision region, in which the dominated error is the unintended single-qubit rotations, e.g., under- or over-rotation (bit-flip error) and an additional single-qubit phase error (phase error) when one focuses on each individual qubit.

In addition, it is worth mentioning that under our definition of gate characterization, we always assume that the other nearby qubit is in the ground or excited state, thereby, the cross-driving induced flip of nearby qubit states contributes to errors of the isolated single-qubit gate, i.e., leading to leakage error. Therefore, the added error per qubit cannot capture the cross-driving induced single-qubit rotation error. As shown in Fig. 4(f), near the Type-1 frequency collision region, although the added error per qubit is rather small, the averaged isolated single-qubit error  $\bar{\varepsilon}_{\text{sum}} = (F_{\blacksquare 0} + F_{0\blacksquare})/2$  is far larger than that for Type-3 frequency region. As we mentioned before, when the qubit system works nearby the Type-1 frequency collision region, the cross-driving effect can lead to unintended single-qubit rotations on one qubit when single-qubit operations are applied to its neighboring qubits. This explains the increase in average gate error  $\bar{\varepsilon}_{\text{sum}}$  when decreasing qubit-qubit detuning. We thus argue that restricted totally to the isolated single-qubit system regardless of nearby qubits states, i.e., tracing out nearby qubits, one can only achieve a nominally high-fidelity single-qubit gate, which cannot account for its practical performance on multi-qubit systems.

Overall, for the present system operated in the straddling regime, the dressing from the qubit-qubit coupling can induce a substantial cross-driving effect, and the associated crosstalk strength (as shown in Figs. 4(c) and 4(d), typically, from

−40 dB to −20 dB) is comparable with that of classical microwave crosstalk [42, 74]. For systems with small qubit-qubit detuning (i.e., near the Type-1 frequency collision region), cross-driving favors bit-flip error or phase error, whereas, for large detuning cases (i.e., near the Type-3 frequency collision region), cross-driving tends to cause leakage error. To ensure high-fidelity single-qubit addressing, the bus-qubit detuning should be large enough, thus bus-mediated exchange coupling is suppressed, and the qubit-qubit detuning should also be away from the frequency collision regions, especially for the Type-1 and Type-3 [69]. Note here that in principle, the direct coupling between qubit and bus can also cause cross-driving from qubit to bus. However, according to Eqs. (5) and (6), one can find  $\epsilon \propto 1/\Delta^3$ , thus, here, the cross-driving effect on the bus is heavily suppressed by the large qubit-bus detuning. This was checked for the present system and was found to be less important.

## 2. two-qubit gate

As demonstrated in Sec. II A, for the present qubit architecture operated in the straddling regime, a high-contrast control over  $ZZ$  interaction can be achieved. When tuning the system energy level  $|101\rangle$  on-resonance with  $|020\rangle$ , i.e., biasing the bus to the working point at  $\omega_{\text{on}} = \bar{\omega} - \eta_{\text{TB}}/2$ , a sub-100-ns CZ gate can be achieved by using diabatic scheme [6, 75] or fast-adiabatic scheme [9, 76–78]. In principle, during the idle time, the system (tunable bus) can be biased to the exact  $ZZ$ -free point. However, as discussed in Sec. II B 1, to have a high fidelity single-qubit addressing, besides residual  $ZZ$  crosstalk, the cross-driving effect should also be minimized. Thus, here the system idle point is chosen so that the typical bus frequency is 500 MHz above the qubit in frequency. In this way, the residual  $ZZ$  coupling can still be suppressed below 10 kHz, as shown in Figs. 1(c) (marked by the black arrow) and 2. Moreover, to avoid the harmful frequency collision in the straddling regime, the qubit-qubit detuning should be located within specific limits, e.g., 100 MHz – 200 MHz, thereby, the single-qubit gate error can be pushed below 0.01% (or even approaches 0.001%), as shown in Fig. 4(f).

In the present qubit architecture, to implement a successful two-qubit gate, several practical experimental limitations also need to be considered seriously:

(1) Uncertainty of system parameters due to fabrication. This is one of the most critical issues faced by fixed-frequency qubits. As shown in Fig. 2, both the available  $ZZ$ -free zone (where the  $ZZ$  coupling strength is below 10 kHz), and the available working zone (where resonance interaction  $|101\rangle \leftrightarrow |020\rangle$  gives rise to a  $ZZ$  coupling with strength about 10 MHz, indicated by black-dashed line labeled by  $\omega_1 + \omega_2 = 2\omega_{\text{TB}} + \eta$ ) in the straddling regime show a promising insensitivity against variation of qubit-qubit detuning and qubit-bus detuning. Thus, the parameter uncertainty issues could be largely fixed by combining this parameter insensitivity and the state-of-the-art fabrication techniques [79, 80].

(2) Gate error resulting from qubit relaxation and dephasing.

Although fixed-frequency transmon qubit itself can have a long coherence time, qubit relaxation rate or dephasing rate can be enhanced through the tunable bus, which is more vulnerable to system noise, especially,  $1/f$  flux noise. Moreover, during the CZ gate operation, a baseband flux pulse is commonly applied to the tunable bus, tuning its frequency from the idle point to the working point. Considering the qubit system shown in Fig. 1, at the working point, the qubit-bus detunings are  $\Delta_1/2\pi = -250$  MHz and  $\Delta_2/2\pi = -50$  MHz. We expect that the small qubit-bus detuning at the working point can cause a strong hybrid between qubit and bus (qubit-bus dressing), especially for  $Q_2$ , thus the qubit relaxation and dephasing through the bus can become greatly serious [9, 60, 77, 78]. For the  $1/f$  noise induced dephasing, this can be mitigated by employing a tunable bus, whose maximum frequency point (i.e., flux-insensitive point) is around the idle point. Therefore, at the idle point, the qubit dephasing through the bus is reduced. Moreover, during CZ gate operations, the needed frequency excursion of the bus is smaller than 500 MHz, thereby potentially greatly reducing flux sensitivity of bus and mitigating the effect of  $1/f$  flux noise [15, 81] (in principle, this could be further improved by using tunable buses with asymmetric SQUID [82]).

(3) Flux pulse distortion. Flux pulse distortion is a critical problem faced by baseband flux controlled gate operations. The presence of flux pulse distortion can cause a substantial gate error, such as leakage error and gate bleedthrough, during CZ gate operations [27, 69, 76, 81]. Although pulse distortion can be largely corrected, one needs to characterize it at first [27]. Unfortunately, in general, one can not directly characterize this distortion without control and measurement of the system subjected to pulse distortion. In qubit architectures with tunable buses or couplers, the bus or coupler, in general, does not have a dedicated driving line and readout resonator. Still, one can put these back, but it will greatly increase circuit complexity [8]. Commonly, due to the presence of (classical or dressed-induced) microwave crosstalk, the bus or coupler can be addressed through the driveline of nearby qubits. However, the readout of bus or coupler state through the readout resonator of nearby qubits is still a challenge. One possible strategy is that combined with the readout of nearby qubits, full control on the bus could be achieved through the qubit-bus interaction [83–85], then the distortion could be corrected [27, 86, 87]. Meanwhile, in the present qubit architecture, the frequency excursion of the bus is small, thereby potentially mitigating the effect of flux setting tails caused by pulse distortion [81, 88].

In the present work, we consider that during the CZ gate operation, a fast adiabatic pulse is applied to the tunable bus, tuning its frequency from the idle point ( $\theta_i$ ) to the working point  $\omega_{\text{on}}$  ( $\theta_f$ ) and then back. Expressed in terms of Fourier basis functions, the pulse shape is described as [76]

$$\theta(t) = \theta_i + \frac{\theta_f - \theta_i}{2} \sum_{n=1,2,3,\dots} \lambda_n \left[ 1 - \cos \frac{2n\pi t}{T} \right] \quad (8)$$

with constraints on the odd coefficients  $\sum_{n \text{ odd}} \lambda_n = 1$ , and control angle  $\theta \equiv \arctan(2J_{101}/\Delta_{101})$ , where  $J_{101}$  denotes

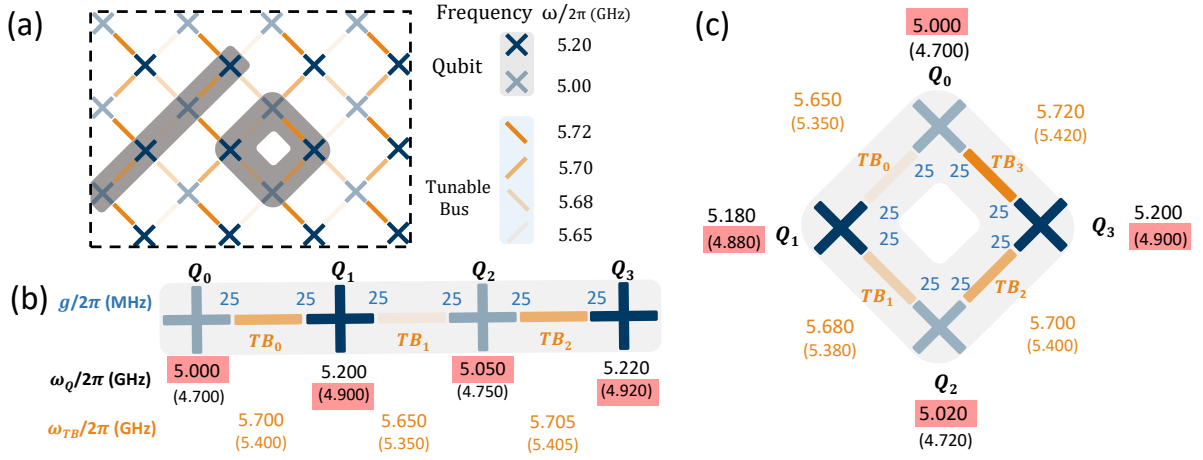


FIG. 5: (a) Layout of a two-dimensional qubit lattice, where cross-shaped vertices (steel-blue) denote qubits, and strip-shaped edges (orange) between adjacent qubits represent tunable buses. Qubits in the lattice belong to one of the two frequency bands, i.e., a lower frequency band with typical frequency  $\omega/2\pi = 5.000$  GHz (light steel-blue) or a higher frequency band with typical frequency  $\omega/2\pi = 5.200$  GHz (dark steel-blue). The typical detuning between nearby qubits is about 200 MHz, and at the idle point, the bus frequency is typically above 500 MHz of the qubits in the higher frequency band. Example of system parameters of four-qubit chain and  $2 \times 2$  four-qubit square shown in the grey shadow of (a) is presented in (b) and (c), respectively, e.g., for  $Q_0$  in the four-qubit chain shown in (b), the qubit frequency is  $\omega_Q/2\pi = 5.000$  GHz, and its anharmonicity is  $-300$  MHz (i.e., its transitions frequency between  $|1\rangle$  and  $|2\rangle$  is 4.700 GHz), the interaction between qubit  $Q_0$  and bus  $TB_0$  is  $g/2\pi = 25$  MHz (at  $\omega_Q/2\pi = \omega_{TB}/2\pi = 5.500$  GHz).

the strength of resonance interaction  $|101\rangle \leftrightarrow |020\rangle$ ,  $\Delta_{101}$  represents the detuning between  $|101\rangle$  and  $|020\rangle$ , and  $T$  is the gate time.

### C. Scaling up to two-dimensional qubit grids

In principle, the above two transmon qubits system can be exploited as building blocks of scalable qubit architectures. An illustration of a 2D qubit lattice, where each transmon qubit is coupled to four nearest neighbors through tunable buses, is shown in Fig. 5(a). In the 2D qubit lattice, the allocation of qubit and bus frequency follows the following rules:

(1) The frequency of the qubit in each row and column belongs to one of the two frequency bands, i.e., a lower frequency band with typical frequency  $\omega/2\pi = 5.000$  GHz and a higher frequency band with typical frequency  $\omega/2\pi = 5.200$  GHz, and qubits in the nearby row or column belong to different frequency bands. Thus, typical detuning between N.N. qubits is about 200 MHz, which is adequate to mitigate cross-driving effect at idle point (Sec. II B) and to implement a sub-100-ns CZ gate, as demonstrated in Sec. II A. Moreover, to mitigate microwave crosstalk impact on qubit addressing between next-nearest-neighbor qubits [27, 69] at the idle point and suppress N.N.N. coupling between qubits at the idle and the working point, frequency degeneracy in the lower- or higher-frequency band breaks, yielding typical qubit detuning between next-nearest-neighbors of about 20 MHz.

(2) To have a better balance between the requirement for suppressing qubit-qubit residual interaction and to limit the frequency excursion range during CZ gate operations, the bus frequency is typically above 500 MHz of the qubit in the

higher frequency band, as shown in Fig. 5(a).

When considering a practical realization of this qubit lattice, frequency uncertainty due to fabrication is the most critical issue, as discussed in Sec. II B 2. Besides striving to improve qubit device fabrication precision [79, 80], one could also try to adopt more sparse qubit connections towards large-scale qubit lattice [80].

## III. QUANTUM CROSSTALK ANALYSIS FOR SIMULTANEOUS GATE OPERATIONS

In this section, we give a quantum crosstalk analysis for simultaneous gate operations on two four-qubit systems shown in Figs. 5(b) and 5(c), where system-specific parameters are also presented. Similar to the discussion in Sec. II B 1, to characterize the quantum crosstalk effect on gate performance, we use the metric of gate fidelity given in Eq. (7). The isolated gate fidelity is obtained by characterizing each gate operation individually with all other non-participating spectator qubits at their ground states, and the simultaneous gate fidelity is obtained by characterizing the parallel implemented gate operations (see Appendix A for details on the calibration procedure). To have enough sensitivity to the added error caused by quantum crosstalk during simultaneous gate operations, each isolated gate is optimized numerically, giving typically isolated single-qubit gate error at  $10^{-6}$  and typical two-qubit CZ gate error at  $10^{-5}$ . Note here that we don't attempt to search for an optimal isolated gate operation with the lowest error, but only for gate operations with enough fidelity, thus enabling an adequate crosstalk sensitivity.

In addition, we note here that in the following dis-



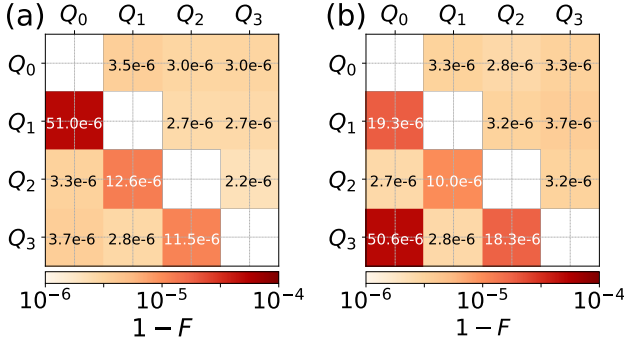


FIG. 6: Gate error of simultaneous single-qubit  $X$  gates (i.e., composite gate  $X \otimes X$ ) applied to arbitrary qubit-pair of (a) the four-qubit chain system and (b) the  $2 \times 2$  four-qubit square system shown in Fig. 5(b) and 5(c). Elements in the upper triangular part of the error matrix denote ideal composite gate error obtained by adding the errors of constituted isolated gates, and elements in the lower triangular parts correspond to the gate error of simultaneous gate operations.

cussion, notations  $|Q_0 Q_1 Q_2 Q_3, TB_0 TB_1 TB_2 TB_3\rangle$  and  $|Q_0 Q_1 Q_2 Q_3, TB_0 TB_1 TB_2\rangle$  represent states of the four-qubit square and four-qubit chain system, respectively. When confined to qubit subspace, notation  $|Q_0 Q_1 Q_2 Q_3\rangle$  is used.

#### A. Simultaneous single-qubit $X$ gate operations

Here, we consider that two 20-ns single-qubit  $X$  gates are applied simultaneously to the arbitrary qubit-pair of the four-qubit system, i.e., implementing a composite  $X$  gate ( $X \otimes X$ ). All tunable buses are tuned to their idle points, thus residual  $ZZ$  interaction between qubits is suppressed below 10 kHz. Same as the discussion in Sec. II B 1, single-qubit gates are realized by using the DRAG scheme with a cosine-shaped pulse.

Figures 6(a) and 6(b) show the error matrix of the parallel implemented  $X$  gates in the four-qubit chain system shown in Fig. 5(b) and the four-qubit square system shown in Fig. 5(c), respectively. Elements in the upper and lower triangular part of the error matrix denote ideal composite gate error obtained by adding the errors of constituted isolated gates and directly characterizing the parallel implemented gate operations, respectively. We find that almost no additional error is observed for the next-nearest-neighbor qubits, and we thus conclude that the quantum crosstalk between next-nearest-neighbor qubits can be neglected. However, focusing on the nearest-neighbor qubit-pairs, the performance of simultaneous gate operations is almost an order of magnitude worse than that of the isolated case.

The above observations are consistent with the analysis of dressing induced cross-driving effect on the gate performance discussed in Sec. II B 1. As interactions between next-nearest-neighbor qubits are commonly an order of magnitude weaker than that of nearest-neighbor qubits, the cross-driving effect can be greatly suppressed. On the contrary, the cross-driving effect between nearest-neighbor qubits cannot

be ignored, and in general can cause a non-negligible error on the simultaneous gate operations. The error can become even more serious when the nearest-neighbor qubit-pair approaches the frequency collision region. For example, focusing on the qubit-pair  $(Q_0, Q_1)$  in the chain system, the detuning between transition  $|0\rangle \leftrightarrow |1\rangle$  of  $Q_0$  and transition  $|1\rangle \leftrightarrow |2\rangle$  of  $Q_1$  (i.e., type-3 frequency collision) takes the smallest value (100 MHz) among all nearby qubits, as marked (in pink shadow) in Fig. 5(b). The closer to the frequency collision region, the more serious the cross-driving error, which can explain that simultaneous  $X$  gate on qubit-pair  $(Q_0, Q_1)$  has the worst gate performance in the four-qubit chain system. Similar results can also be obtained for the qubit-pair  $(Q_0, Q_3)$  in the square system.

In addition, note that as discussed in Sec. II B 1, cross-driving induced single-qubit rotation error has been taken into account already for the characterization of the isolated gate performance, and can lead to leakage error since we always assume all the non-participating spectator qubit in their ground states. However, during simultaneous single-qubit gate operations, this rotation error occurs within the two-qubit computational subspace, thus here it does not contribute to the leakage error but the control error for the composite gate operation. The combination of decreased leakage error and increased control error can explain that for the next-nearest-neighbor qubit-pair, whose detuning approaches the Type-1 frequency collision (as discussed in Sec. II B 1, here the cross-driving effect favors single-qubit rotation error), the ideal composite gate appears to have a little bit larger gate error than that of the simultaneous gate operation, as shown in Fig. 6(a) (we have checked this independency, and find that without consideration of leakage error, this feature indeed disappears).

To give a more concrete illustration of the cross-driving impact on the present four-qubit system, Figures 7(a) and 7(b) show the  $X$  gate error with the other three spectator qubits in four different state-configurations for the four-qubit chain and square system, respectively. Generally, we find that compared with the isolated gate operation, gate error is increased when a state flip of one nearby qubit occurs. Moreover, qubits in the lower-frequency band show a more prominent decrease in gate performance, such as  $Q_0$  in the two four-qubit systems. This is to be expected, as detuning between the transition  $|0\rangle \leftrightarrow |1\rangle$  of the qubit in the lower-frequency band and the transition  $|1\rangle \leftrightarrow |2\rangle$  of one in the higher-frequency band, typically, 100 MHz, is smaller than that in the reversed case, typically, 500 MHz. Thus, the cross-driving effect from the low-frequency qubit to the nearby high-frequency qubit is more serious and can result in leakage error for the low-frequency qubit. In Figs. 7(c) and 7(d), we also show the time evolution of state population during  $X_{Q_0}$  with one of  $Q_0$ 's nearby qubit in its excited state. For the four-qubit system initialized in  $|0100\rangle$ , we find that during  $X$  gate on  $Q_0$ , the qubit  $Q_1$  state can be excited from  $|1\rangle$  to  $|2\rangle$  (see Figs. 7(c) and 7(d),  $P_{0200}$  and  $P_{1200}$ ), accounting for the dominated leakage error  $Leak_{0100} \equiv 1 - (P_{0100} + P_{1100})$ . Similarly, for the four-qubit square system prepared in  $|0001\rangle$ , the leakage error  $Leak_{0001} \equiv 1 - (P_{0001} + P_{1001})$  is mainly resulted

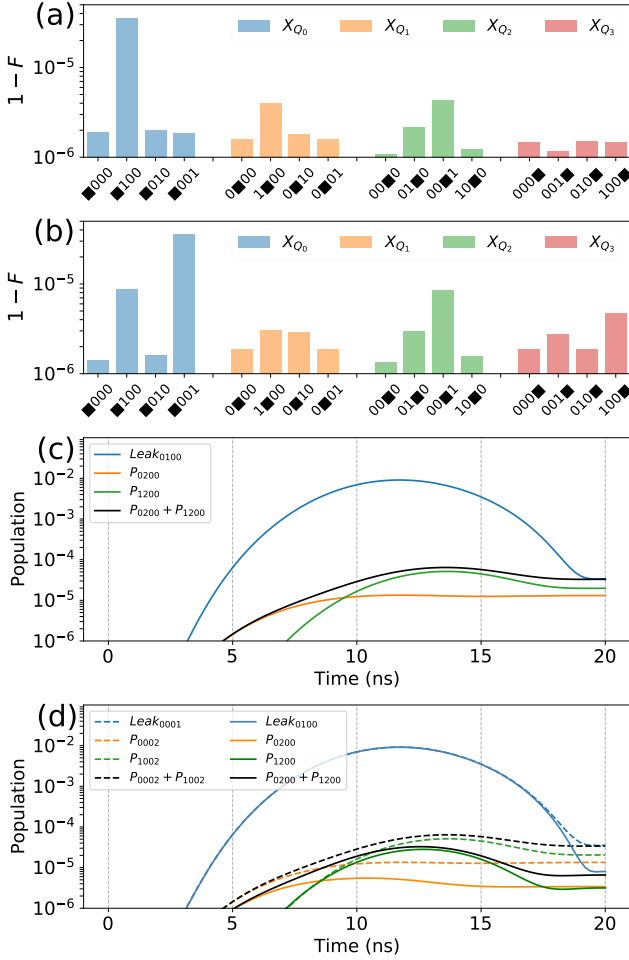


FIG. 7:  $X$  gate error with the other three spectator qubits in four different state-configurations, e.g., marked by  $\{\blacksquare 000, \blacksquare 100, \blacksquare 010, \blacksquare 001\}$  for  $Q_0$ . (a) for the four-qubit chain system shown in Fig. 5(b). (b) for the four-qubit square system shown in Fig. 5(c). (c) and (d) State population as a function of time during the isolated single-qubit operations in the four-qubit chain system and square system. Solid lines (dashed lines) denote the result for the four-qubit system initialized in  $|0100\rangle$  ( $|0001\rangle$ ). The leakages are defined as  $Leak_{0100} = 1 - (P_{0100} + P_{1100})$ ,  $Leak_{0001} = 1 - (P_{0001} + P_{1001})$ , where  $P_{ijkl}$  represents the population in the four-qubit state  $|ijkl\rangle$ .

from the population leakage of  $Q_3$  (see Fig. 7(d), dashed line). Overall, the above analysis shows that the dressed induced cross-driving can explain the performance degradation of simultaneous gate operations applied to qubit-pair  $(Q_0, Q_1)$  in the four-qubit chain system and  $(Q_0, Q_3)$  in the four-qubit square system.

Before leaving this subsection, we note that although the cross-driving effect can cause almost an order of magnitude worse gate performance in the above illustration, on average the added gate error is about  $10^{-5}$ , which is an order of magnitude lower than the state-of-the-art gate performance [3–5]. However, when qubit systems approach the frequency-

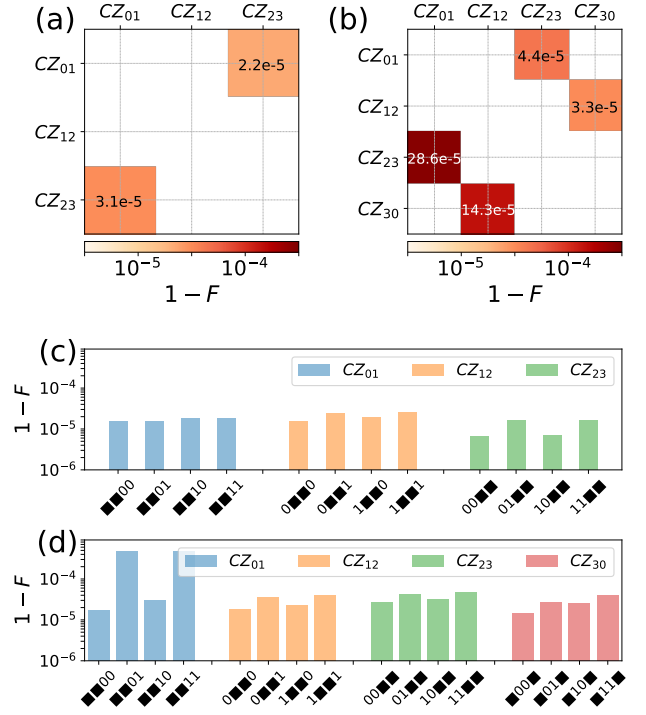


FIG. 8: Error Matrix of simultaneous CZ gates in (a) the four-qubit chain system and (b) the four-qubit square system. (c) and (d) CZ gate error with the other two nonparticipating qubits in four different state-configurations (i.e., 00, 01, 10, 11) for the four-qubit chain system and the four-qubit square system.

collision region or have a larger inter-qubit coupling at the idle point, this cross-driving effect can become a dominant error source for simultaneous single-qubit gate operations. This suggests that the cross-driving effect should be taken seriously into account to design and construct a large multi-qubit lattice.

## B. Simultaneous two-qubit CZ gate operations

In this subsection, we turn to examine the performance of simultaneous CZ gates in the two four-qubit systems shown in Figs. 5(b) and 5(c). Similar to the analysis of the single-qubit case, we consider that individual CZ gate is tuned up and characterized with the other two nonparticipating qubits in their ground states. During gate operations, except for the bus to which a baseband flux pulse is applied for realizing a CZ gate, the other buses are all biased to their idle points. The CZ gate is implemented by using a fast-adiabatic pulse given in Eq. (8) with three Fourier coefficients  $\{\lambda_1, \lambda_2, \lambda_3\}$ , giving rise to totally three free parameters  $\{\lambda_1, \lambda_2, \theta_f\}$ . The other parameters are: gate time  $T = 68$  ns,  $J_{101}/2\pi = 12$  MHz. For reaching a given target error at  $10^{-5}$ , the three free parameters are fixed using numerical optimization (see Appendix A 2 for details).

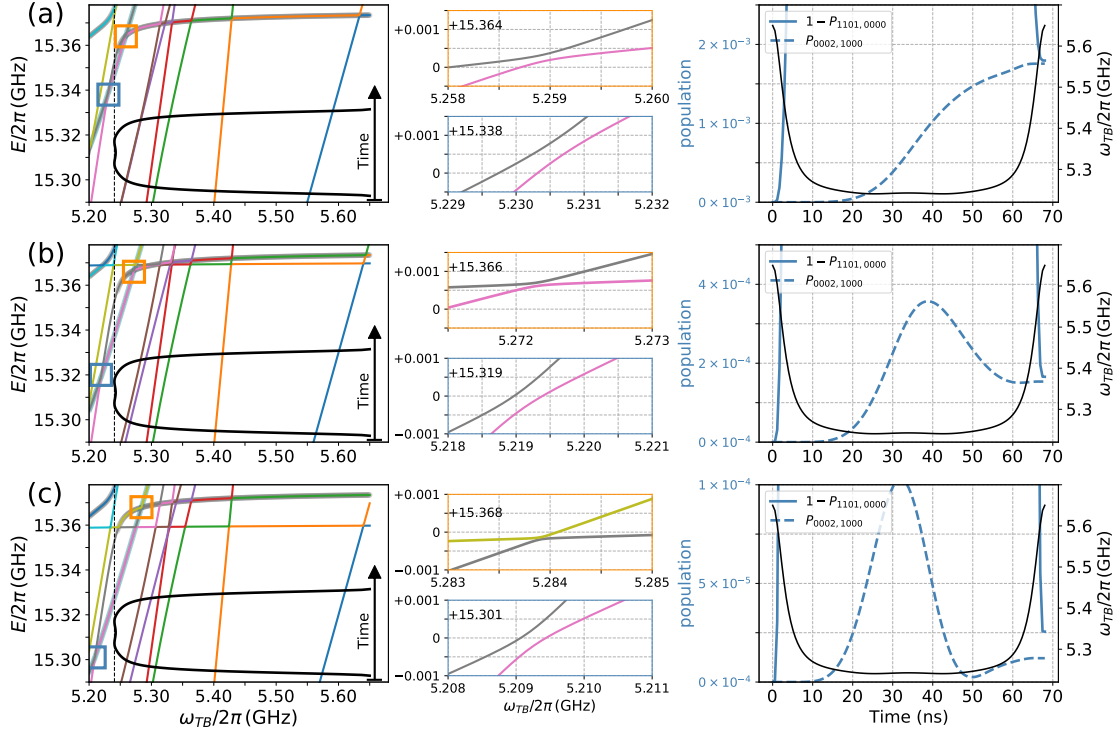


FIG. 9: (left panel) Energy-level spectrum of the four-qubit square system shown in Fig. 5. The dashed black line indicates the working point, and the orange (steel-blue) square marks the avoided crossing resulting from interaction  $|1101, 0000\rangle \leftrightarrow |0002, 1000\rangle$  and  $|0001, 2000\rangle \leftrightarrow |0002, 1000\rangle$ , respectively, which are highlighted in the middle panel. (right panel) Time evolution of state population during the implementation of  $CZ_{01}$  with system prepared in the state  $|1101, 0000\rangle$ .  $P_{1101,0000}$  and  $P_{0002,1000}$  denote the population on state  $|1101, 0000\rangle$  and state  $|0002, 1000\rangle$ . The black curves in (left panel) and (right panel) represent the 68-ns shaped pulse used to realize  $CZ_{01}$ . (a) Qubit anharmonicities are  $\eta_Q/2\pi = -300$  MHz. (b) Qubit anharmonicities are  $\eta_Q/2\pi = -310$  MHz. (c) Qubit anharmonicities are  $\eta_Q/2\pi = -320$  MHz. Other parameters are the same as in Fig. 5(c).

### 1. gate performance

In Figs. 8(a) and 8(b), we show simultaneous CZ gate performance in the four-qubit chain system and four-qubit square system. In the chain system, the added error of simultaneous CZ gates is about  $10^{-5}$ , giving an average added error  $0.5 \times 10^{-5}$  for the individual CZ gate, and in the four-qubit square system, the added error is about  $2.4 \times 10^{-4}$  and  $1.1 \times 10^{-4}$  for gate pairs  $\{CZ_{01}, CZ_{23}\}$  and  $\{CZ_{12}, CZ_{30}\}$ , respectively, which are about an order of magnitude larger than that of the isolated case. Given the state-of-the-art two-qubit gate performance, although it appears likely that the quantum crosstalk between the gate pair  $\{CZ_{01}, CZ_{23}\}$  in the chain system is less important, the quantum crosstalk effect on the square system can become a near-term performance limiting factor. Thus, in the following discussion, we can restrict our attention to the square system in which the quantum crosstalk effect is more prominent.

To explore the exact nature of the performance degradation, Figures 8(c) and 8(d) show the CZ gate error with the other two nonparticipating qubits in four different state-configurations for the chain system and square system, respectively. One can find that except for  $CZ_{01}$  in the square system,

gate errors of all the CZ gates show only a weak size dependence on the state of nonparticipating qubits. Typically, here the added error is about  $10^{-5}$ . However, in the square system, when  $Q_3$  is in the excited state, the gate error of  $CZ_{01}$  is increased by about a factor of 28, giving rise to an added error of  $4.5 \times 10^{-4}$ .

To explain the above striking increase in the gate error, we have examined the time evolution of the square system during  $CZ_{01}$  with  $Q_3$  prepared in its excited state. We find that the leakage error, which is caused by the high-order parasitic interaction among  $|1101, 0000\rangle$ ,  $|0002, 1000\rangle$  and  $|0001, 2000\rangle$ , can account for the added gate error, as illustrated in Fig. 9(a). From the energy spectrum of the four-qubit square system in the left panel of Fig. 9(a), there exists two avoided crossings resulting from interaction  $|1101, 0000\rangle \leftrightarrow |0002, 1000\rangle$  and  $|0001, 2000\rangle \leftrightarrow |0002, 1000\rangle$ , which are on either side of the working point at  $\omega_{\text{on}} \simeq 5.240$  GHz. Thus, when a flux pulse tunes the bus to the working point and then comes back according to the fast-adiabatic pulse given in Eq. (8), the system will first sweep through the avoided crossing ( $|1101, 0000\rangle \leftrightarrow |0002, 1000\rangle$ ) at 5.2590 GHz, and then approaches the avoided crossing ( $|0001, 2000\rangle \leftrightarrow |0002, 1000\rangle$ ) at 5.2305 GHz, as shown in the middle panel of Fig. 9(a). In

the right panel of Fig. 9(a), where the time evolution of state population is presented, we find that leakage to  $|0002, 1000\rangle$  mainly occurs when the system approaches the avoided crossing at 5.2305 GHz.

Before giving a more detailed analysis of the leakage error, we note that during an ideal fast adiabatic CZ gate operation, the qubit system should always be in the instantaneous eigenstates of the qubit system. For the system initialized in  $|1101, 0000\rangle$ , the system dynamics should be restricted in the subspace spanned by  $\{|1101, 0000\rangle, |0001, 2000\rangle\}$ . In light of this, the above observation can be explained by that as the flux-pulse has a short-time ramp (right panel of Fig. 9(a), black line), and the energy gap of the avoided crossing at 5.2590 GHz is about 250 kHz, the system can thus sweep through it with a negligible leakage to  $|0002, 1000\rangle$ . However, during the main part of the flux-pulse that has a flat shape, the system is almost settled at the working point, where the instantaneous eigenstates is an almost maximal superposition state of  $|1101, 0000\rangle$  and  $|0001, 2000\rangle$ . Moreover, the working point nears the second avoided crossing with a tiny energy gap of 500 kHz at 5.2305 GHz, in which the detuning to the working point is about 10 MHz. Thus, an off-resonance population swap between  $|0002, 1000\rangle$  and  $|0001, 2000\rangle$  occurs, causing significant leakage to  $|0002, 1000\rangle$ . Note here that during the main part of the flux-pulse, the off-resonance population swap between  $|1101, 0000\rangle$  and  $|0002, 1000\rangle$  can also occur due to the avoided crossing at 5.2590 GHz. However, as its detuning to the working point is about 20 MHz and its gap is 250 kHz, the leakage resulting from the off-resonance interaction between  $|1101, 0000\rangle$  to  $|0002, 1000\rangle$  is expected to be far less than that from the off-resonance interaction between  $|0001, 2000\rangle$  and  $|0002, 1000\rangle$ .

The above analysis suggests that although individual gate operations with high gate fidelity can be achieved, implementing the gate operation in parallel can show substantial performance degradation. Moreover, in multiqubit systems, there can exist detrimental high-order parasitic interactions that cannot be captured by only characterizing isolated gate operations with all other nonparticipating qubits in their ground states. On the contrary, characterizing gate operations with other nonparticipating qubits at different state configurations may give further insight into the quantum crosstalk behind the performance degradation of the simultaneous gate operations [55].

## 2. mitigation of parasitic interaction involving spectator qubits

From the above, the leakage to state  $|0002, 1000\rangle$  is the dominated error source for  $CZ_{01}$  with  $Q_3$  in its excited state. Here, we intend to mitigate such errors from the hardware perspective. As the leakage is mainly caused by the existence of the parasitic interaction (i.e.,  $|1101, 0000\rangle \leftrightarrow |0002, 1000\rangle$  and  $|0001, 2000\rangle \leftrightarrow |0002, 1000\rangle$ ) around the working point, here we intend to push them away from the working point. As shown in the left panel of Figs. 9(b) and 9(c), due to the increase of qubit anharmonicities, the energy of state  $|0001, 2000\rangle$  is lowered, thereby, the avoided crossings re-

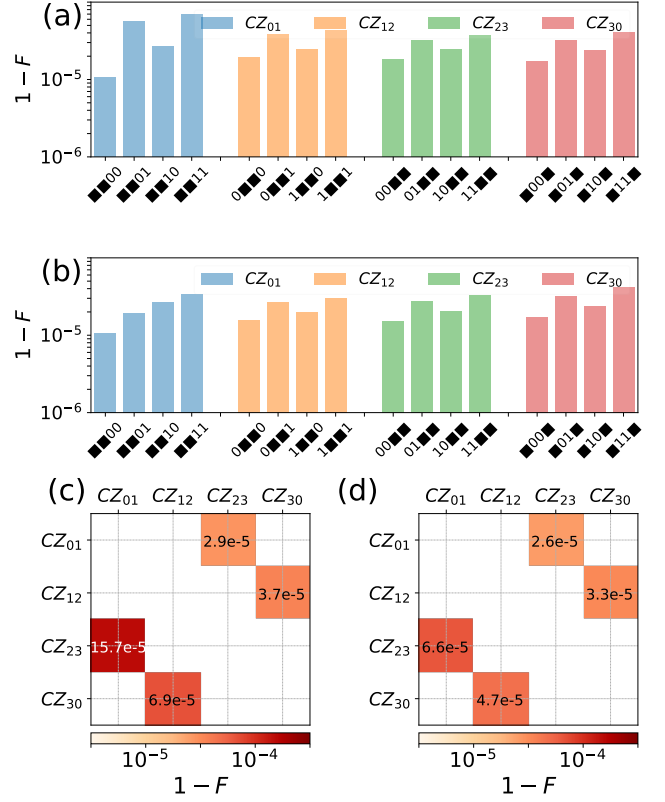


FIG. 10: (a) and (b) CZ gate error with the other two nonparticipating qubits in four different state-configurations (i.e., 00, 01, 10, 11) for the four-qubit square system. (c) and (d) Error matrix of the parallel implemented CZ gate operations in the four-qubit square system. In (a) and (c), the qubit anharmonicity is  $\eta_Q/2\pi = -310$  MHz. In (b) and (d), the qubit anharmonicity is  $\eta_Q/2\pi = -320$  MHz. The other system parameters are the same as those in Fig. 5(c).

sulting from the parasitic interactions are far away from the working point. In this way, due to the increased detuning from state  $|0002, 1000\rangle$ , the off-resonance population swap between state  $|0001, 2000\rangle$  and state  $|0002, 1000\rangle$  can be suppressed. Thus, as shown in the right panel of Figs. 9(b) and 9(c), the leakage to  $|0002, 1000\rangle$  is indeed greatly reduced, in line with expectation. Note that this is similar to the incomplete Rabi oscillation resulting from an off-resonance driving, and the population error can be roughly estimated by Eq. (6).

Given the suppression of the leakage error, Fig. 10(a) and Fig. 10(b) show the isolated gate fidelity of  $CZ_{01}$  with qubit anharmonicity  $\eta_Q/2\pi = -310$  MHz and qubit anharmonicity  $\eta_Q/2\pi = -320$  MHz, respectively. The gate errors of  $CZ_{01}$  with  $Q_3$  in its excited state are indeed greatly decreased in both cases. In particular, for the case of  $\eta_Q/2\pi = -320$  MHz, there is no fundamental difference between the gate error of the CZ gate on different qubit-pairs, and gate errors of all pairs show a weak dependence on the state of the nonparticipating qubits. On average, the added error for each operation is suppressed below  $2 \times 10^{-5}$ . Figures 10(c) and 10(d)



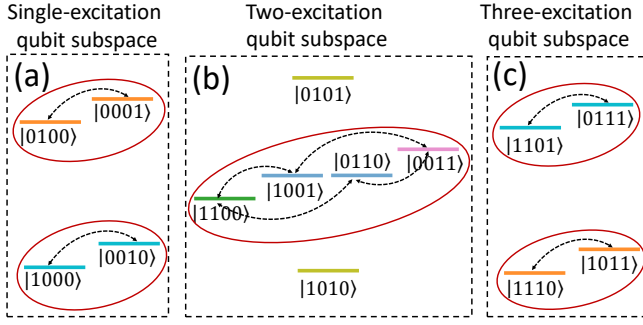


FIG. 11: Next-nearest-neighbor interaction in (a) single-excitation subspace (b) two-excitation subspace (c) three-excitation subspace. In the four-qubit system shown in Fig. 5, the typical detuning between next-nearest-neighbor qubits is 20 MHz. During the CZ gate operation, a flux pulse tunes the tunable bus from the idle point to the working point, the bus energy levels will push down the qubit energy levels, thus potentially diminishing the detuning between next-nearest-neighbor qubits and leading to population swap (double-headed arrow) between next-nearest-neighbor qubits.

also present the error matrix of simultaneous CZ gates. We find that compared to the result shown in Fig. 8(b), where  $\eta_Q/2\pi = -300$  MHz, on average the added error of the parallel implemented CZ gates is suppressed twofold for the square system with  $\eta_Q/2\pi = -310$  MHz, and sixfold for  $\eta_Q/2\pi = -320$  MHz.

Besides the leakage error, the remaining error could be attributed to the parasitic interactions between next-nearest-neighbor qubits. As shown in Fig. 11, parasitic swap interactions (double-headed arrow) among single-excitation, two-excitation, and three-excitation subspace can exist through high-order processes. Since the typical detuning between next-nearest-neighbor qubits is 20 MHz (see Fig. 5), when a flux pulse tunes the tunable bus from the idle point to the working point, the bus energy levels will push down the qubit energy levels, thus potentially diminishing the detuning between next-nearest-neighbor qubits and leading to population swap between next-nearest-neighbor qubits. Thanks to the rather small qubit-bus coupling, the population swap can be suppressed below  $10^{-4}$  (this was checked for the four-qubit square system prepared in  $2^4$  different qubit-state-configurations, see Appendix B for details). In principle, this can be further improved by increasing the detuning between next-nearest-neighbor qubits. This suggests that for systems with increased qubit-bus or qubit-coupler coupling, as the energy level shift is also increased, thereby, to ensure high-fidelity simultaneous gates, a large detuning between next-nearest-neighbor qubits is needed.

### 3. leakage from the avoid-crossing with a tiny gap

We end this section by showing that without the consideration of qubit decoherence, there could exist a performance trade-off between isolated two-qubit gate operations and si-

multaneous two-qubit gate operations, i.e., in general, isolated gate operations with slower gate-speed can suppress parasitic interactions within target qubit systems, but for simultaneous gate operations, fast-speed gates could mitigate parasitic interactions associated with nonparticipating spectator qubits. In Fig. 12, the solid line represents the isolated  $CZ_{01}$  gate error with the other two nonparticipating qubits prepared in two different state-configurations, i.e.,  $1 - F_{\blacksquare\blacksquare 00}$  and  $1 - F_{\blacksquare\blacksquare 01}$ , versus gate time in the four-qubit square system shown in Fig. 5(c). In general, we find that isolated gates with slow-speed have a lower error, but the increased gate error of  $CZ_{01}$  with  $Q_3$  in the excited state and the leakage to state  $|0002, 1000\rangle$ , i.e.,  $P_{0002, 1000}$ , suggest that the gate error of simultaneous gate operations becomes serious.

To further elucidate the general physics behind the trade-off, we consider that the present four-qubit system can be simplified to a multi-anticrossing system that comprises a main avoided crossing with a dominated energy gap (at the working point) and several avoided crossings with tiny energy gaps (this is in general different from the parasitic interaction within target qubit systems, in which the strength of the parasitic interactions is comparable to or even larger than that of the desired interaction, thereby, the working point is chosen so that it is far detuned from the parasitic resonance points). The main avoided crossing results from the desired interaction used for realizing gate operations, e.g., the interaction between  $|1101, 0000\rangle$  and  $|0001, 2000\rangle$ , and the tiny avoided crossing comes from high-order parasitic interaction, e.g., interaction between  $|1101, 0000\rangle$  and  $|0002, 1000\rangle$ , and interactions between next-nearest-neighbor qubits, as shown in Fig. 11. In Fig. 13, we show two different situations that correspond to the two error sources discussed in Sec. III B 2:

(i) as shown in Fig. 13(a), there is a tiny avoided crossing resulting from the interaction between  $|j\rangle$  and  $|\alpha\rangle$ . Generally, to implement a gate operation, one needs to bias the system to the working point. Therefore, during the operation, the system will sweep through this tiny avoided crossing and then come back. Thus, sweeping through this avoided crossing with fast-speed could suppress leakage to state  $|j\rangle$ .

(ii) as shown in Fig. 13(b), around the working point, a tiny avoided crossing, i.e., labeled as  $k$ , exists, corresponding to the parasitic interaction point (resulting from the coupling between  $|\gamma\rangle$  and  $|k\rangle$ ). During the gate operation, the system approaches the parasitic resonance point, thus the detuning between  $|\gamma\rangle$  and  $|k\rangle$  is reduced. In addition, the energy level  $|\gamma\rangle$  is pushed down due to its coupling to the state  $|\alpha\rangle$ , thereby, further reducing its detuning from  $|k\rangle$ . Ideally, the system dynamics should be restricted in the subspace spanned by  $\{|\alpha\rangle, |\gamma\rangle\}$ . However, the off-resonance interaction between the  $|\gamma\rangle$  and  $|k\rangle$  can result in an incomplete population swap between the two states, especially, when the detuning between  $|\gamma\rangle$  and  $|k\rangle$  becomes smaller, a population swap with a larger magnitude will present, thus potentially causing non-negligible control or leakage error (here, i.e. leakage to the state  $|k\rangle$ ). Note that the same as the off-resonance error in single-qubit systems [70], in general, the off-resonance swap can be suppressed by increasing the detuning between the two states, as demonstrated in Sec. III B 2. Furthermore, the ex-

act off-resonance swap error should be studied by considering the shape and the gate-time of the control pulse [8, 70, 81]. In general, pulses with a long ramp can mitigate the off-resonance swap error. Moreover, the error itself exhibits a periodic dependence on the gate time, and the period generally is inversely proportional to the detuning. As shown in Fig. 12, the dashed line denotes the isolated  $CZ_{01}$  gate error versus gate time with an increased qubit anharmonicity  $\eta_Q/2\pi = -310$  MHz, giving a larger detuning between state  $|0002, 1000\rangle$  and state  $|0001, 2000\rangle$  (Fig. 9(b), about 20 MHz). Compared to the case of  $\eta_Q/2\pi = -300$  MHz (see Fig. 13, solid lines), we can find that due to the increased detuning, both the magnitude of leakage to state  $|0002, 1000\rangle$  and the time of the oscillation period are decreased as expected. Thus, to mitigate the off-resonance error, particular attention should be paid to the parasitic resonance point (where a tiny avoided crossing exists) with a small detuning to the working point. In this case, the smaller the detuning, the longer the period of the error oscillation, thereby, implementing a gate operation within a short time can mitigate the off-resonance swap error (see Fig. 12, solid lines).

To circumvent the detrimental effect from these tiny-gap avoided crossings, on the whole, we argue that implementing short gates or pushing away these avoided-crossings could greatly relieve the population leakage and swap process involving parasitic next-nearest-neighbor interactions. However, fast-speed gate operations are commonly realized with potentially increased gate error within target qubit systems, such as the leakage error [81]. In the present qubit architecture, to suppress diabatic transitions within the target two-qubit system, the gate-length cannot be reduced below 50 ns, limited by the small qubit-bus coupling. This could raise a tread-off between gate error resulting from target qubit systems themselves and error from non-participating spectator qubits, as shown in Fig. 12. With regard to engineering quantum systems to remove harmful tiny-gap avoided crossings, although its success has been demonstrated in the four-qubit square system (see Sec. III B 2), it is still an open question as to whether this will prove useful in a large qubit lattice.

#### IV. CONCLUSION AND DISCUSSION

In this work, we first propose a qubit architecture with tunable  $ZZ$  coupling, where fixed-frequency transmon qubits are coupled via a tunable bus, and sub-100-ns CZ gates can be realized by applying a fast-adiabatic flux-pulse to the bus. Then, we thoroughly analyze the quantum crosstalk impact on simultaneous gate operations in this qubit architecture. In general, we find that characterization of isolated gate errors, especially, with all non-participating spectator qubits in their ground states, cannot capture the full physical picture of error sources behind simultaneous gate operations. Given this insight, we examine the isolated gate performance with non-participating spectator qubits in various state configurations. Combining with an inspection of the system dynamics during gate operations, we find that to ensure high simultaneous single-qubit gate fidelities, dressing-induced cross-

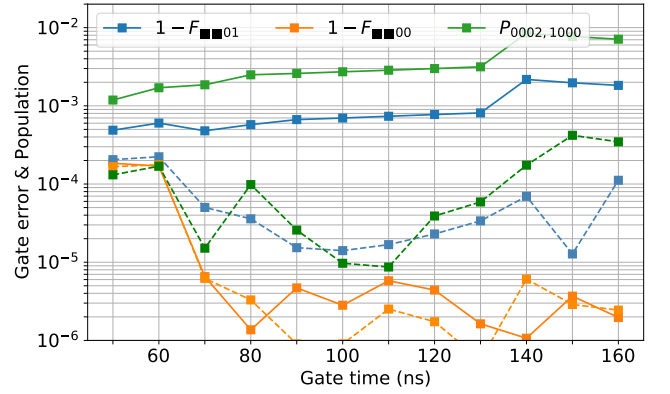


FIG. 12: Isolated  $CZ_{01}$  gate error with the other two nonparticipating qubits in two different state-configurations, i.e.,  $1 - F_{0001}$  and  $1 - F_{0000}$ , as a function of gate time.  $P_{0002,1000}$  denotes the population leakage to state  $|0002, 1000\rangle$  with the four-qubit square system initialized in state  $|1101, 0000\rangle$ . Solid lines and dashed lines denote the result with qubit anharmonicity  $\eta_Q/2\pi = -300$  MHz and  $\eta_Q/2\pi = -310$  MHz, respectively. The other system parameters used here are the same as in Fig. 5(c).

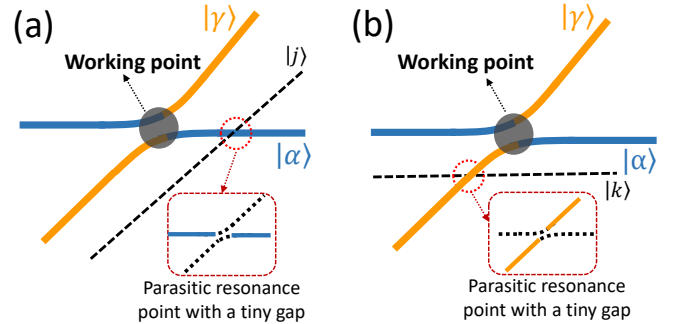


FIG. 13: Leakage channel in a multi-anticrossing system comprising a main avoided crossing (resulting from the resonance interaction between  $|\alpha\rangle$  and  $|\gamma\rangle$ ) with a dominated energy gap (working point) and an avoided crossing involving (a)  $|j\rangle$  or (b)  $|k\rangle$  with a tiny energy gap. In (a) during gate operations, the system will sweep through the parasitic resonance point, potentially causing leakage to state  $|j\rangle$  and in (b) the system will approach the parasitic resonance point, resulting in a population swap between  $|k\rangle$  and  $|\gamma\rangle$ .

driving should be seriously considered when one operates qubits near the frequency collision regions. For simultaneous two-qubit gates, while parasitic nearest-neighbor interactions are commonly suppressed, parasitic next-nearest-neighbor interactions involving spectator qubit can still exist, causing considerable leakage or control error when qubit systems sweep through or approach these parasitic resonance points slowly. As gate operations with slower speed can, in general, suppress unwanted interactions within target qubit systems, but for high-order parasitic interactions involving spectator qubits, one tends to favor short gates. This could give rise to a trade-off between the error resulting from target

qubit systems themselves and the error from non-participating spectator qubits. Thus, our analysis suggests that in pursuit of a functional quantum processor, the qubit architecture should be examined carefully in the context of high-fidelity simultaneous gate operations.

To mitigate the dominated high-order parasitic interaction in the proposed qubit architecture, we also consider a hardware approach to mitigating their detrimental effect. We demonstrate that by engineering qubit parameters, we can push these parasitic resonance points far away from the working point of desired interaction. In this way, on average, there is almost an order of magnitude improvement in gate performance, giving the added error for simultaneous CZ gates below  $1.5 \times 10^{-5}$ . The remaining error could be further suppressed by increasing the detuning between next-nearest-neighbor qubits. This suggests that the proposed qubit architecture may be a potential architecture towards a large-scale superconducting quantum processor with low quantum crosstalk.

Although our present analysis of quantum crosstalk focuses on superconducting qubit architecture with tunable buses, we expect that many of our conclusions may also be applied to other qubit architecture, such as the qubit architecture with tunable coupler [9, 12, 41, 77, 81], and or at the very least, may give some physical insight into the exact nature of quantum crosstalk in these qubit architectures. Meanwhile, the analysis procedure may also provide a preliminary guideline for analyzing quantum crosstalk in other qubit architecture, and may help motivate future work on bridging the gap between high-level, hardware-agnostic crosstalk characterization [19] and the exact nature of crosstalk.

### Acknowledgments

We would like to thank Yanwu Gu, Mengjun Hu, Yingshan Zhang, Jingning Zhang, and Teng Ma for many helpful discussions. We also thank Yu Song and Shuang Yang for helpful suggestions on the manuscript. This work was supported by the Beijing Natural Science Foundation (Grant No.Z190012), the National Natural Science Foundation of China (Grants No.11890704, No.12004042, No.11905100), the National Key Research and Development Program of China (Grant No.2016YFA0301800), and the Key-Area Research and Development Program of Guang Dong Province (Grant No. 2018B030326001). P.X. was supported by the Young Fund of Jiangsu Natural Science Foundation of China (Grant No.BK20180750) and the National Natural Science Foundation of China (Grant No.12105146).

### Appendix A: calibration procedure of gate operations

In this Appendix, we gave further detailed descriptions on the calibration procedure of gate operations (i.e., single-qubit X gate and two-qubit CZ gate) discussed in the main text. Here, for illustration purposes only, we consider the two-qubit system shown in Fig. 1. In the following discussion, we show

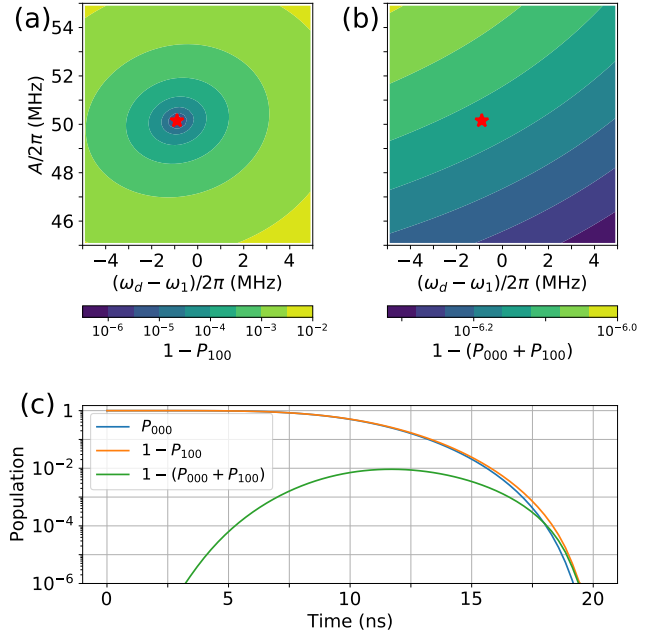


FIG. 14: Tune-up procedure for the single-qubit X gate. (a) Population error  $1 - P_{100}$  as a function of the driving amplitude  $A$  and the driving detuning  $(\omega_d - \omega_1)$  for the two-qubit system initialized in state  $|000\rangle$ , and the fixed gate length  $t_g = 20$  ns. (b) Same as in (a), instead of showing the leakage  $1 - (P_{000} + P_{100})$  versus the driving amplitude  $A$  and the driving detuning  $(\omega_d - \omega_1)$  for the single-qubit gate operations. (c) System dynamics during the gate operation with the optimal parameter set indicated by the red stars in (a-b) where both the population error and the leakage are suppressed below  $10^{-6}$ .

how the single-qubit X gate and the two-qubit CZ gate are calibrated in the two-qubit system. As in Fig. 1, the system parameters are: qubit frequency  $\omega_{1(2)}/2\pi = 5.000(5.200)$  GHz, anharmonicity  $\eta_1 = \eta_2 = \eta_{TB} = \eta$  ( $\eta/2\pi = -300$  MHz), and qubit-bus coupling  $g_{1(2)} = g$  ( $g/2\pi = 25$  MHz) (at  $\omega_{1(2)} = \omega_{TB} = 5.500$  GHz). In addition, the idle point of the tunable bus is at  $\omega_{TB}/2\pi = 5.65$  GHz, as marked by the black arrow in Fig. 1(c). In the following discussion, notations  $|Q_1 Q_2 TB\rangle$  represent the full system states, and when confined to the qubit subspace, notation  $|Q_1 Q_2\rangle$  is used.

In addition, we note that the following introduced calibration procedures are also applied to the calibration of single-qubit gates and two-qubit gates in the four-qubit system studied in Sec. III.

#### 1. Calibration of single-qubit X gates

As we mentioned in Sec. II B 1, in the present work, the single-qubit X gate is implemented by using the DRAG scheme [3, 4, 71]. For illustration purposes, here, we consider the implementation of a single-qubit X gate applied to the qubit  $Q_1$ . As shown in Eq. 4, the driven Hamiltonian for

implementing  $X_{Q_1}$  is

$$\begin{aligned} H_d(t) &= [\Omega_x(t) \cos(\omega_d t) + \Omega_y(t) \sin(\omega_d t)](a_1^\dagger + a_1), \\ \Omega_x(t) &= \frac{A}{2}[1 - \cos(2\pi t/t_g)], \Omega_y(t) = -\frac{\alpha}{\eta} \dot{\Omega}_x(t), \end{aligned} \quad (\text{A1})$$

The  $X_{Q_1}$  gate is tuned up by adjusting the driving amplitude  $A$  and the driving detuning of the pulse from the qubit bare frequency ( $\omega_d - \omega_1$ ) for a fixed gate length ( $t_g = 20$  ns) and the parameter  $\alpha = 0.5$ . Figure 14(a) shows the population error  $1 - P_{100}$  ( $P_{100}$  denotes the population in state  $|100\rangle$  at the end of the gate operation) as a function of the driving amplitude  $A$  and the driving detuning ( $\omega_d - \omega_1$ ) for the two-qubit system initialized in state  $|000\rangle$ . In Fig. 14(b), we also show the leakage error  $1 - (P_{000} + P_{100})$ . One can find that at the minimal error point, i.e.,  $\{A/2\pi \simeq 50.15$  MHz,  $(\omega_d - \omega_1)/(2\pi) \simeq 0.9$  MHz $\}$ , marked by the red stars in Figs. 14(a) and (b), both the population error and leakage is suppressed below  $10^{-6}$ , as shown in Fig. 14(c). Note here that in the present setting, as expected, the obtained optimal driving frequency is indeed at the dressed qubit frequency of  $Q_1$ .

After obtaining the optimal parameter set from the result shown in Fig. 14, we characterize the fidelity of  $X_{Q_1}$  gate by using the metric given in Eq. 7, i.e.,

$$F(\tilde{U}_X, X) = \frac{\text{Tr}(\tilde{U}_X^\dagger \tilde{U}_X) + |\text{Tr}(X^\dagger \tilde{U}_X)|^2}{6}, \quad (\text{A2})$$

where  $\tilde{U}_X$  denote the actual implemented X gate operation, and

$$X = \begin{pmatrix} 0 & 1 \\ 1 & 0 \end{pmatrix}. \quad (\text{A3})$$

According to the two-qubit system Hamiltonian given in Eq. 1 and the driven Hamiltonian given in Eq. A1, the actual evolution operator is

$$U_1 = \hat{T} \exp \left( -i \int_0^{t_g} H_X(t) dt \right), \quad (\text{A4})$$

where  $H_X(t) = H + H_d(t)$ , and  $\hat{T}$  denotes the time-ordering operator. Thus, in the single-qubit computational subspace for  $Q_1$ , the actual implemented X gate operation is given as

$$\tilde{U}_X = \mathcal{P}_1 U_1 \mathcal{P}_1^\dagger, \quad (\text{A5})$$

where  $\mathcal{P}_1$  is the projected operator defined in the computational subspace of the full system, i.e., the subspace spanned by  $\{|000\rangle, |100\rangle\}$ . Finally, to account for the local single-qubit phase [3, 4], the gate fidelity is obtained as [43, 46]

$$F = \text{maximize}_{\{\phi\}} F(U_{\text{post1}}(\phi) \tilde{U}_X, X), \quad (\text{A6})$$

with  $U_{\text{post1}}(\phi) = e^{-i\phi Z/2}$ , where  $Z$  represents the single-qubit Pauli operator  $\sigma_z$ .

## 2. Calibration of CZ gates

As mentioned in Sec. II B 2 and Sec. III B, the CZ gate

$$CZ = \begin{pmatrix} 1 & 0 & 0 & 0 \\ 0 & 1 & 0 & 0 \\ 0 & 0 & 1 & 0 \\ 0 & 0 & 0 & -1 \end{pmatrix} \quad (\text{A7})$$

is realized by applying a fixed-length ( $T = 68$  ns) flux pulse to the tunable bus, tuning its frequency from its idle point ( $\theta_0$ ) to the working point ( $\theta_f$ ) and then coming back. The pulse shape is given in Eq. 8 with three Fourier coefficients  $\{\lambda_1, \lambda_2, \lambda_3\}$ , where  $\lambda_1 + \lambda_3 = 1$ . Thus, this gives rise to totally three free parameters  $\{\lambda_1, \lambda_2, \theta_f\}$ . For reaching a target error at around  $10^{-5}$ , the free parameter set is determined by optimizing the CZ gate fidelity according to the metric given in Eq. 7, i.e.,

$$F(\tilde{U}_{cz}, CZ) = \frac{\text{Tr}(\tilde{U}_{cz}^\dagger \tilde{U}_{cz}) + |\text{Tr}(CZ^\dagger \tilde{U}_{cz})|^2}{20}. \quad (\text{A8})$$

Similar to the case of single-qubit gates, according to the system Hamiltonian given in Eq. 1 and the pulse shape given in Eq. 8, the actual evolution operator for the gate operation is

$$U_2 = \hat{T} \exp \left( -i \int_0^T H(t) dt \right). \quad (\text{A9})$$

Thus, truanted to the two-qubit computational subspace, the actual implemented CZ gate operation is given as

$$\tilde{U}_{cz} = \mathcal{P}_2 U_2 \mathcal{P}_2^\dagger, \quad (\text{A10})$$

where  $\mathcal{P}_2$  is the projected operator defined in the two-qubit subspace spanned by  $\{|000\rangle, |010\rangle, |100\rangle, |110\rangle\}$ . Finally, to account for the local single-qubit phases [43, 46], the gate fidelity is obtained as

$$F = \text{maximize}_{\{\phi_1, \phi_2\}} F(U_{\text{post2}}(\phi_1, \phi_2) \tilde{U}_{cz}, CZ), \quad (\text{A11})$$

with  $U_{\text{post2}}(\phi_1, \phi_2) = e^{-i\phi_1 Z I/2} e^{-i\phi_2 I Z/2}$ , where  $Z$  and  $I$  represent the single-qubit Pauli operator  $\sigma_z$  and identity operators, and the order indexes the qubit number.

## Appendix B: population swap between next-nearest-neighboring qubits

As shown in Fig. 11 and mentioned in Sec. II B 2, the population swap between next-nearest-neighbor qubit pairs which results from off-resonance interaction among them in the four-qubit system, can contribute to the gate error of simultaneous CZ gates. Figure 15 shows the population swap matrix  $P(o|i)$  in the single-excitation subspace  $\{|1000\rangle, |0010\rangle, |0100\rangle, |0001\rangle\}$ , the two-excitation subspace  $\{|1100\rangle, |1001\rangle, |0110\rangle, |0011\rangle\}$ , and the three-excitation subspace  $\{|1110\rangle, |1011\rangle, |1101\rangle, |0111\rangle\}$  of the four-qubit square system shown in Fig. 5(c). Each matrix element  $P(o|i)$  denotes the population in state  $|o\rangle$  after the gate operation with the qubit system initialized in state  $|i\rangle$ .



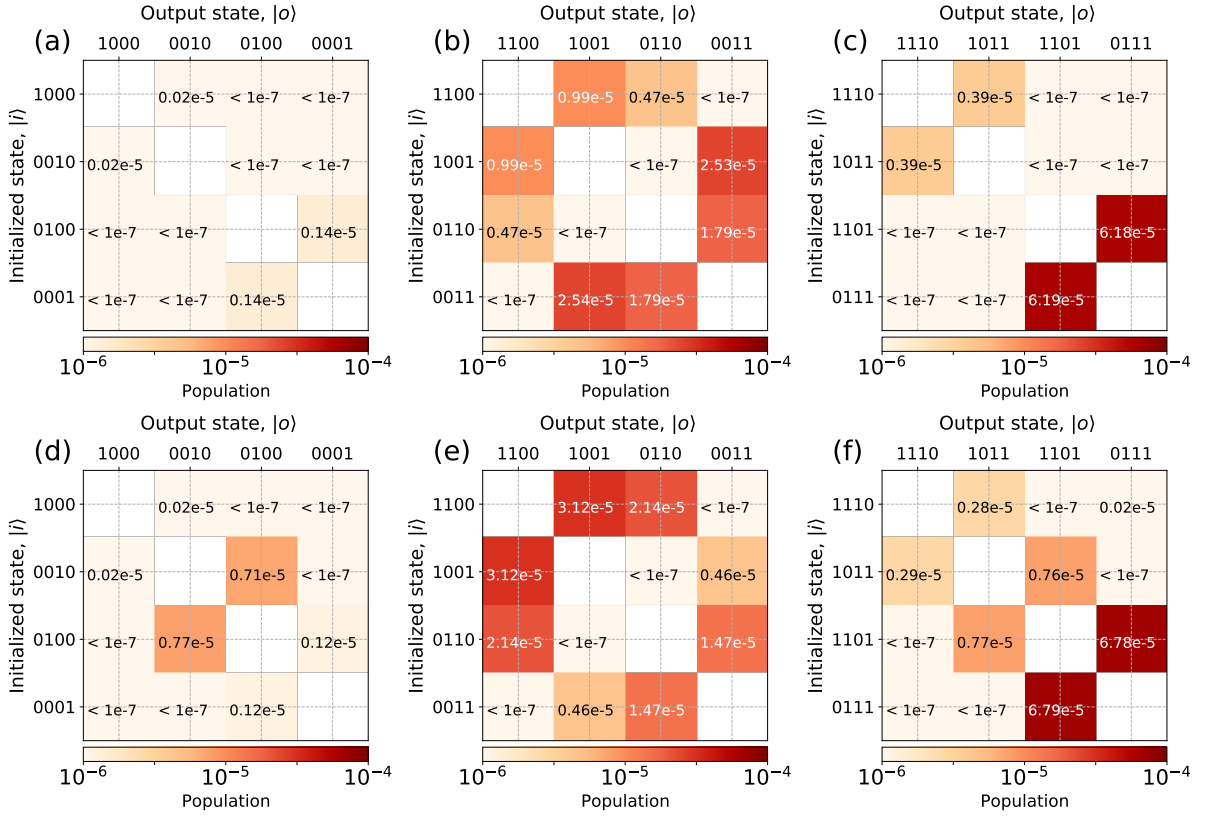


FIG. 15: Population swap matrix  $P(o|i)$  for the implementation of simultaneous CZ gates in the four-qubit square system shown in Fig. 5(c). The matrix element  $P(o|i)$  denotes the population in state  $|o\rangle$  for the qubit system initialized in state  $|i\rangle$ . [(a),(d)] for the qubit system initialized in the single-excitation subspace  $\{|1000\rangle, |0010\rangle, |0100\rangle, |0001\rangle\}$ , [(b),(e)] for the two-excitation subspace  $\{|1100\rangle, |1001\rangle, |0110\rangle, |0011\rangle\}$ , and [(c),(f)] for the three-excitation subspace  $\{|1110\rangle, |1011\rangle, |1101\rangle, |0111\rangle\}$ . (a-c) Population swap matrix for the parallel implementation of  $CZ_{01}$  and  $CZ_{23}$ . (d-f) Population swap matrix for the parallel implementation of  $CZ_{12}$  and  $CZ_{30}$ .

From Fig. 15, one can find that a significant population swap only exists for the state transition process involving next-nearest-neighbor qubits. These transitions are indicated by double-headed arrows connecting the states of next-

nearest-neighbor qubits, as shown in Fig. 11. Moreover, as these population swaps are enabled by high-order processes, the population swap errors are suppressed below  $10^{-4}$ .

- 
- [1] J. M. Martinis, Qubit Metrology for Building a Fault Tolerant Quantum Computer, *npj Quantum Inf.* **1**, 15005 (2015).
  - [2] M. Kjaergaard, M. E. Schwartz, J. Braumüller, P. Krantz, J. I.-J. Wang, S. Gustavsson, and W. D. Oliver, Superconducting qubits: Current state of play, *Annu. Rev. Condens. Matter Phys.* **11**, 369 (2020).
  - [3] Z. Chen, J. Kelly, C. Quintana, R. Barends, B. Campbell, Y. Chen, B. Chiaro, A. Dunsworth, A. G. Fowler, E. Lucero, E. Jeffrey, A. Megrant, J. Mutus, M. Neeley, C. Neill, P. J. J. ÓMalley, P. Roushan, D. Sank, A. Vainsencher, J. Wenner, T. C. White, A. N. Korotkov, and J. M. Martinis, Measuring and Suppressing Quantum State Leakage in a Superconducting Qubit, *Phys. Rev. Lett.* **116**, 020501 (2016).
  - [4] D. C. McKay, C. J. Wood, S. Sheldon, J. M. Chow, and J. M. Gambetta, Efficient z gates for quantum computing, *Phys. Rev. A* **96**, 022330 (2017).
  - [5] A. Somoroff, Q. Ficheux, R. A. Mencia, H. Xiong, R. V. Kuzmin, and V. E. Manucharyan, Millisecond coherence in a superconducting qubit, *arXiv:2103.08578*.
  - [6] R. Barends, C. M. Quintana, A. G. Petukhov, Y. Chen, D. Kafri, K. Kechedzhi et al., Diabatic Gates for Frequency-Tunable Superconducting Qubits, *Phys. Rev. Lett.* **123**, 210501 (2019).
  - [7] M. A. Rol, F. Battistel, F. K. Malinowski, C. C. Bultink, B. M. Tarasinski, R. Vollmer, N. Haider, N. Muthusubramanian, A. Bruno, B. M. Terhal, and L. DiCarlo, Fast, High-Fidelity Conditional-Phase Gate Exploiting Leakage Interference in Weakly Anharmonic Superconducting Qubits, *Phys. Rev. Lett.* **123**, 120502 (2019).
  - [8] Y. Sung, L. Ding, J. Braumüller, A. Vepsäläinen, B. Kannan, M. Kjaergaard, A. Greene, G. O. Samach, C. McNally, D. Kim, A. Melville, B. M. Niedzielski, M. E. Schwartz, J. L. Yoder, T. P. Orlando, S. Gustavsson, and W. D. Oliver, Realization of High-

- Fidelity CZ and ZZ-Free iSWAP Gates with a Tunable Coupler, *Phys. Rev. X* **11**, 021058 (2021).
- [9] Y. Xu, J. Chu, J. Yuan, J. Qiu, Y. Zhou, L. Zhang, X. Tan, Y. Yu, S. Liu, J. Li, F. Yan, and D. Yu, High-Fidelity, High-Scalability Two-Qubit Gate Scheme for Superconducting Qubits, *Phys. Rev. Lett.* **125**, 240503 (2020).
- [10] B. K. Mitchell, R. K. Naik, A. Morvan, A. Hashim, J. M. Kreikebaum, B. Marinelli, W. Lavrijsen, K. Nowrouzi, D. I. Santiago, and I. Siddiqi, Hardware-Efficient Microwave-Activated Tunable Coupling Between Superconducting Qubits, *arXiv:2105.05384*.
- [11] K. X. Wei, E. Magesan, I. Lauer, S. Srinivasan, D. F. Bogorin, S. Carnevale, G. A. Keefe, Y. Kim, D. Klaus, W. Landers, N. Sundaresan, C. Wang, E. J. Zhang, M. Steffen, O. E. Dial, D. C. McKay, and A. Kandala, Quantum crosstalk cancellation for fast entangling gates and improved multi-qubit performance, *arXiv:2106.00675*.
- [12] E. A. Sete, N. Didier, A. Q. Chen, S. Kulshreshtha, R. Manenti, and S. Poletto, Parametric-Resonance Entangling Gates with a Tunable Coupler, *Phys. Rev. Applied* **16**, 024050 (2021).
- [13] Q. Ficheux, L. B. Nguyen, A. Somoroff, H. Xiong, Ko. N. Nesterov, M. G. Vavilov, and V. E. Manucharyan, Realization of Fast Logic with Slow Qubits: Microwave-Activated Controlled-Z Gate on Low-Frequency Fluxoniums, *Phys. Rev. X* **11**, 021026 (2021).
- [14] J. M. Chow, S. J. Srinivasan, E. Magesan, A. D. Córcoles, D. W. Abraham, J. M. Gambetta, and M. Steffen, Characterizing a four-qubit planar lattice for arbitrary error detection, *Proc. SPIE* **9500**, Quantum Inf. Comput. **13**, 95001G (2015).
- [15] F. Arute, K. Arya, R. Babbush, D. Bacon, J. C. Bardin, R. Barends, R. Biswas, S. Boixo, F. G. Brandao, D. A. Buell *et al.*, Quantum supremacy using a programmable superconducting processor, *Nature* **574**, 505 (2019).
- [16] Q. Zhu, S. Cao, F. Chen, M.-C. Chen, X. Chen, T.-H. Chung, H. Deng, Y. Du, D. Fan, M. Gong *et al.*, Quantum Computational Advantage via 60-Qubit 24-Cycle Random Circuit Sampling, *arXiv:2109.03494*.
- [17] X. Zhang, W. Jiang, J. Deng, K. Wang, J. Chen, P. Zhang, W. Ren, H. Dong, S. Xu, Y. Gao, F. Jin, X. Zhu, Q. Guo, H. Li, C. Song, Z. Wang, D.-L. Deng, and H. Wang, Observation of a symmetry-protected topological time crystal with superconducting qubits, *arXiv:2109.05577*.
- [18] D. M. Zajac, J. Stehlik, D. L. Underwood, T. Phung, J. Blair, S. Carnevale, D. Klaus, G. A. Keefe, A. Carniol, M. Kumph, M. Steffen, O. E. Dial, Spectator Errors in Tunable Coupling Architectures, *arXiv:2108.11221*.
- [19] M. Sarovar, T. Proctor, K. Rudinger, K. Young, E. Nielsen, and R. Blume-Kohout, Detecting crosstalk errors in quantum information processors, *Quantum* **4**, 321 (2020).
- [20] A. G. Fowler, M. Mariantoni, J. M. Martinis, and A. N. Cleland, Surface codes: Towards practical large-scale quantum computation, *Phys. Rev. A* **86**, 032324 (2012).
- [21] J. M. Gambetta, A. D. Córcoles, S. T. Merkel, B. R. Johnson, John A. Smolin, J. M. Chow, C. A. Ryan, C. Rigetti, S. Poletto, T. A. Ohki, M. B. Ketchen, and M. Steffen, Characterization of Addressability by Simultaneous Randomized Benchmarking, *Phys. Rev. Lett.* **109**, 240504 (2012).
- [22] K. Rudinger, T. Proctor, D. Langharst, M. Sarovar, K. Young, and R. Blume-Kohout, Probing Context-Dependent Errors in Quantum Processors, *Phys. Rev. X* **9**, 021045 (2019).
- [23] C. Huang, X. Ni, F. Zhang, M. Newman, D. Ding, X. Gao, T. Wang, H. Zhao, F. Wu, G. Zhang, C. Deng, H. Ku, J. Chen, and Y. Shi, Alibaba Cloud Quantum Development Platform: Surface Code Simulations with Crosstalk, *arXiv:2002.08918*.
- [24] S. Niu and A. Todri-Sanial, Analyzing crosstalk error in the NISQ era, *arXiv:2106.01671*.
- [25] A. Ash-Saki, M. Alam, and S. Ghosh, Experimental Characterization, Modeling, and Analysis of Crosstalk in a Quantum Computer, *IEEE Transactions on Quantum Engineering* **1**, 1 (2021).
- [26] K. Rudinger, C. W. Hogle, R. K. Naik, A. Hashim, D. Lobser, D. I. Santiago, M. D. Grace, E. Nielsen, T. Proctor, S. Seritan, S. M. Clark, R. Blume-Kohout, I. Siddiqi, and K. C. Young, Experimental Characterization of Crosstalk Errors with Simultaneous Gate Set Tomography, *arXiv:2103.09890*.
- [27] R. Barends, J. Kelly, A. Megrant, A. Veitia, D. Sank, E. Jeffrey, T. C. White, J. Mutus, A. G. Fowler, B. Campbell, Y. Chen, Z. Chen, B. Chiaro, A. Dunsworth, C. Neill, P. O'Malley, P. Roushan, A. Vainsencher, J. Wenner, A. N. Korotkov, A. N. Cleland, and J. M. Martinis, Superconducting quantum circuits at the surface code threshold for fault tolerance, *Nature* **508**, 500 (2014).
- [28] D. M. Abrams, N. Didier, S. A. Caldwell, B. R. Johnson, and C. A. Ryan, Methods for Measuring Magnetic Flux Crosstalk between Tunable Transmons, *Phys. Rev. Applied* **12**, 064022 (2019).
- [29] X. Dai, D. M. Tennant, R. Trappen, A. J. Martinez, D. Melanson, M. A. Yurtalan, Y. Tang, S. Novikov, J. A. Grover, S. M. Disseler, J. I. Basham, R. Das, D. K. Kim, A. J. Melville, B. M. Niedzielski, S. J. Weber, J. L. Yoder, D. A. Lidar, and A. Lupascu, Calibration of flux crosstalk in large-scale flux-tunable superconducting quantum circuits, *arXiv:2105.14360*.
- [30] M. Takita, A. D. Córcoles, E. Magesan, B. Abdo, M. Brink, A. Cross, J. M. Chow, and J. M. Gambetta, Demonstration of Weight-Four Parity Measurements in the Surface Code Architecture, *Phys. Rev. Lett.* **117**, 210505 (2016).
- [31] M. Takita, A. W. Cross, A. D. Córcoles, J. M. Chow, and J. M. Gambetta, Experimental Demonstration of Fault-tolerant State Preparation with Superconducting Qubits, *Phys. Rev. Lett.* **119**, 180501 (2017).
- [32] D. C. McKay, S. Sheldon, J. A. Smolin, J. M. Chow, and J. M. Gambetta, Three Qubit Randomized Benchmarking, *Phys. Rev. Lett.* **122**, 200502 (2019).
- [33] N. Sundaresan, I. Lauer, E. Pritchett, E. Magesan, P. Jurcevic, and J. M. Gambetta, Reducing Unitary and Spectator Errors in Cross Resonance with Optimized Rotary Echoes, *PRX Quantum* **1**, 020318 (2020).
- [34] A. Winick, J. J. Wallman, and J. Emerson, Simulating and Mitigating Crosstalk, *Phys. Rev. Lett.* **126**, 230502 (2021).
- [35] X. Deng, Y. Hai, J. Li, and Y. Song, Correcting correlated errors for quantum gates in multi-qubit systems using smooth pulse control, *arXiv:2103.08169*.
- [36] V. Tripathi, H. Chen, M. Khezri, K. Yip, E. M. Levenson-Falk, and D. A. Lidar, Suppression of crosstalk in superconducting qubits using dynamical decoupling, *arXiv:2108.04530*.
- [37] P. Murali, D. C. McKay, M. Martonosi, and A. Javadi-Abhari, Software Mitigation of Crosstalk on Noisy Intermediate-Scale Quantum Computers, *arXiv:2001.02826*.
- [38] Y. Ding, P. Gokhale, S. F. Lin, R. Rines, T. Propson, and F. T. Chong, Systematic Crosstalk Mitigation for Superconducting Qubits via Frequency-Aware Compilation, *arXiv:2008.09503*.
- [39] K. N. Smith, G. S. Ravi, P. Murali, J. M. Baker, N. Earnest, A. Javadi-Abhari, and F. T. Chong, Error Mitigation in Quantum Computers through Instruction Scheduling, *arXiv:2105.01760*.
- [40] Y. Chen, C. Neill, P. Roushan, N. Leung, M. Fang, R. Barends, J. Kelly, B. Campbell, Z. Chen, B. Chiaro, A. Dunsworth, E. Jeffrey, A. Megrant, J. Y. Mutus, P. J. J. O'Malley, C. M. Quintana, D. Sank, A. Vainsencher, J. Wenner, T. C. White, M. R.

- Geller, A. N. Cleland, and J. M. Martinis, Qubit architecture with high coherence and fast tunable coupling, *Phys. Rev. Lett.* **113**, 220502 (2014).
- [41] F. Yan, P. Krantz, Y. Sung, M. Kjaergaard, D. L. Campbell, T. P. Orlando, S. Gustavsson, and W. D. Oliver, Tunable Coupling Scheme for Implementing High-Fidelity Two-Qubit Gates, *Phys. Rev. Applied* **10**, 054062 (2018).
- [42] A.D. Patterson, J. Rahamim, T. Tsunoda, P.A. Spring, S. Jebari, K. Ratter, M. Mergenthaler, G. Tancredi, B. Vlastakis, M. Esposito, and P.J. Leek, Calibration of a Cross-Resonance Two-Qubit Gate Between Directly Coupled Transmons, *Phys. Rev. Applied* **12**, 064013 (2019).
- [43] P. Zhao, P. Xu, D. Lan, X. Tan, H. Yu, and Y. Yu, Switchable Next-Nearest-Neighbor Coupling for Controlled Two-Qubit Operations, *Phys. Rev. Applied* **14**, 064016 (2020).
- [44] P. S. Mundada, G. Zhang, T. Hazard, and A. A. Houck, Suppression of Qubit Crosstalk in a Tunable Coupling Superconducting Circuit, *Phys. Rev. Applied* **12**, 054023 (2019).
- [45] J. Ku, X. Xu, M. Brink, D. C. McKay, J. B. Hertzberg, M. H. Ansari, and B. L. T. Plourde, Suppression of Unwanted ZZ Interactions in a Hybrid Two-Qubit System, *Phys. Rev. Lett.* **125**, 200504 (2020).
- [46] P. Zhao, P. Xu, D. Lan, J. Chu, X. Tan, H. Yu, and Y. Yu, High-Contrast ZZ Interaction Using Superconducting Qubits with Opposite-Sign Anharmonicity, *Phys. Rev. Lett.* **125**, 200503 (2020).
- [47] X. Xu and M.H. Ansari, ZZ freedom in two qubit gates, *Phys. Rev. Applied* **15**, 064074 (2021).
- [48] A. Kandala, K. X. Wei, S. Srinivasan, E. Magesan, S. Carnevale, G. A. Keefe, D. Klaus, O. Dial, and D. C. McKay, Demonstration of a High-Fidelity CNOT for Fixed-Frequency Transmons with Engineered ZZ Suppression, *arXiv:2011.07050*.
- [49] P. Zhao, D. Lan, P. Xu, G. Xue, M. Blank, X. Tan, H. Yu, and Y. Yu, Suppression of Static ZZ Interaction in an All-Transmon Quantum Processor, *Phys. Rev. Applied* **16**, 024037 (2021).
- [50] A. D. K. Finck, S. Carnevale, D. Klaus, C. Scerbo, J. Blair, T. G. McConkey, C. Kurter, A. Carniol, G. Keefe, M. Kumph, and O.E. Dial, Suppressed crosstalk between two-junction superconducting qubits with mode-selective exchange coupling, *arXiv:2105.11495*.
- [51] A. Noguchi, A. Osada, S. Masuda, S. Kono, K. Heya, S. P. Wolski, H. Takahashi, T. Sugiyama, D. Lachance-Quirion, and Y. Nakamura, Fast parametric two-qubit gates with suppressed residual interaction using the second-order nonlinearity of a cubic transmon, *Phys. Rev. A* **102**, 062408 (2020).
- [52] A. Petrescu, C. L. Calonnec, C. Leroux, A. D. Paolo, P. Mundada, S. Sussman, A. Vrajitoarea, A. A. Houck, and A. Blais, Accurate methods for the analysis of strong-drive effects in parametric gates, *arXiv:2107.02343*.
- [53] C. Leroux, A. D. Paolo, and A. Blais, Superconducting coupler with exponentially large on-off ratio, *arXiv:2107.09861*.
- [54] X. Li, T. Cai, H. Yan, Z. Wang, X. Pan, Y. Ma, W. Cai, J. Han, Z. Hua, X. Han, Y. Wu, H. Zhang, H. Wang, Yipu Song, Luming Duan, and Luyan Sun, Tunable Coupler for Realizing a Controlled-Phase Gate with Dynamically Decoupled Regime in a Superconducting Circuit, *Phys. Rev. Applied* **14**, 024070 (2020).
- [55] S. Krinner, S. Lazar, A. Remm, C.K. Andersen, N. Lacroix, G.J. Norris, C. Hellings, M. Gabureac, C. Eichler, and A. Wallraff, Benchmarking Coherent Errors in Controlled-Phase Gates due to Spectator Qubits, *Phys. Rev. Applied* **14**, 024042 (2020).
- [56] M. Malekakhlagh, E. Magesan, and D. C. McKay, First-principles analysis of cross-resonance gate operation, *Phys. Rev. A* **102**, 042605 (2020).
- [57] T.-Q. Cai, X.-Y. Han, Y.-K. Wu, Y.-L. Ma, J.-H. Wang, Z.-L. Wang, H.-Y. Zhang, H.-Y. Wang, Y.-P. Song, and L.-M. Duan, Impact of Spectators on a Two-Qubit Gate in a Tunable Coupling Superconducting Circuit, *Phys. Rev. Lett.* **127**, 060505 (2021).
- [58] J. Chu and F. Yan, Coupler-Assisted Controlled-Phase Gate with Enhanced Adiabaticity, *arXiv:2106.00725*.
- [59] J. Koch, T. M. Yu, J. Gambetta, A. A. Houck, D. I. Schuster, J. Majer, A. Blais, M. H. Devoret, S. M. Girvin, and R. J. Schoelkopf, Charge-insensitive qubit design derived from the cooper pair box, *Phys. Rev. A* **76**, 042319 (2007).
- [60] D. C. McKay, S. Filipp, A. Mezzacapo, E. Magesan, J. M. Chow, and J. M. Gambetta, Universal gate for fixed-frequency qubits via a tunable bus, *Phys. Rev. Applied* **6**, 064007 (2016).
- [61] R. Krishnan and J. A. Pople, Approximate fourth-order perturbation theory of the electron correlation energy, *Int. J. Quantum Chem.* **14**, 91 (1978).
- [62] L. DiCarlo, J. M. Chow, J. M. Gambetta, L. S. Bishop, B. R. Johnson, D. I. Schuster, J. Majer, A. Blais, L. Frunzio, S. M. Girvin, and R. J. Schoelkopf, Demonstration of two-qubit algorithms with a superconducting quantum processor, *Nature (London)* **460**, 240 (2009).
- [63] L. Jin, Implementing High-fidelity Two-Qubit Gates in Superconducting Coupler Architecture with Novel Parameter Regions, *arXiv:2105.13306*.
- [64] M. H. Goerz, F. Motzoi, K. B. Whaley, and C. P. Koch, Charting the circuit QED design landscape using optimal control theory, *npj Quantum Information* **3**, 37 (2017).
- [65] G. S. Paraoanu, Microwave-induced coupling of superconducting qubits, *Phys. Rev. B* **74**, 140504(R) (2006).
- [66] C. Rigetti and M. Devoret, Fully microwave-tunable universal gates in superconducting qubits with linear couplings and fixed transition frequencies, *Phys. Rev. B* **81**, 134507 (2010).
- [67] E. Magesan and J. M. Gambetta, Effective Hamiltonian models of the cross-resonance gate, *Phys. Rev. A* **101**, 052308 (2020).
- [68] M. Brink, J. M. Chow, J. Hertzberg, E. Magesan, and Sami Rosenblatt, Device challenges for near term superconducting quantum processors: frequency collisions, *2018 IEEE International Electron Devices Meeting (IEDM)*, (2018).
- [69] J. Kelly, R. Barends, B. Campbell, Y. Chen, Z. Chen, B. Chiaro, A. Dunsworth, A. G. Fowler, I.-C. Hoi, E. Jeffrey, A. Megrant, J. Mutus, C. Neill, P. J. J. ÓMalley, C. Quintana, P. Roushan, D. Sank, A. Vainsencher, J. Wenner, T. C. White, A. N. Cleland, and J. M. Martinis, Optimal Quantum Control Using Randomized Benchmarking, *Phys. Rev. Lett.* **112**, 240504 (2014).
- [70] M. Malekakhlagh and E. Magesan, Mitigating off-resonant error in the cross-resonance gate, *arXiv:2108.03223*.
- [71] F. Motzoi, J. M. Gambetta, P. Rebentrost, and F. K. Wilhelm, Simple Pulses for Elimination of Leakage in Weakly Nonlinear Qubits, *Phys. Rev. Lett.* **103**, 110501 (2009).
- [72] L. H. Pedersen, N. M. Møller, and K. Mølmer, Fidelity of quantum operations, *Phys. Lett. A* **367**, 47 (2007).
- [73] C. J. Wood and J. M. Gambetta, Quantification and characterization of leakage errors, *Phys. Rev. A* **97**, 032306 (2018).
- [74] S. Huang, B. Lienhard, G. Calusine, A. Vepsäläinen, J. Braumüller, D. K. Kim, A. J. Melville, B. M. Niedzielski, J. L. Yoder, B. Kannan, T. P. Orlando, S. Gustavsson, and W. D. Oliver, Microwave Package Design for Superconducting Quantum Processors, *PRX Quantum* **2**, 020306 (2021).
- [75] K. Linghu *et al.*, in preparation. (2020).
- [76] J. M. Martinis and M. R. Geller, Fast adiabatic qubit gates using only  $\sigma^z$  control, *Phys. Rev. A* **90**, 022307 (2014).
- [77] M. C. Collodo, J. Herrmann, N. Lacroix, C. K. Andersen, A.

- Remm, S. Lazar, J. Besse, T. Walter, A. Wallraff, and C. Eichler, Implementation of Conditional Phase Gates Based on Tunable ZZ Interactions, *Phys. Rev. Lett.* **125**, 240502 (2020).
- [78] J. Stehlik, D. M. Zajac, D.L. Underwood, T. Phung, J. Blair, S. Carnevale, D. Klaus, G. A. Keefe, A. Carniol, M. Kumph, M. Steffen, and O. E. Dial, Tunable Coupling Architecture for Fixed-Frequency Transmon Superconducting Qubits, *Phys. Rev. Lett.* **127**, 080505 (2021).
- [79] J. M. Kreikebaum, K. P. O'Brien, A. Morvan, and I. Siddiqi, Improving wafer-scale Josephson junction resistance variation in superconducting quantum coherent circuits, *Supercond. Sci. Technol.* **33**, 06LT02 (2020).
- [80] J. B. Hertzberg, E. J. Zhang, S. Rosenblatt, E. Magesan, J. A. Smolin, J.-B. Yau, V. P. Adiga, M. Sandberg, M. Brink, Je. M. Chow, and J. S. Orcutt, Laser-annealing Josephson junctions for yielding scaled-up superconducting quantum processors, *npj Quantum Information* **7**, 129 (2021).
- [81] B. Foxen, C. Neill, A. Dunsworth, P. Roushan, B. Chiaro, A. Megrant, J. Kelly, Z. Chen, K. Satzinger, R. Barends *et al.*, Demonstrating a Continuous Set of Two-Qubit Gates for Near-Term Quantum Algorithms, *Phys. Rev. Lett.* **125**, 120504 (2020).
- [82] M. D. Hutchings, J. B. Hertzberg, Y. Liu, N. T. Bronn, G. A. Keefe, M. Brink, J. M. Chow, and B. L. T. Plourde, Tunable Superconducting Qubits with Flux-Independent Coherence, *Phys. Rev. Applied* **8**, 044003 (2017).
- [83] P. J. Leek, S. Filipp, P. Maurer, M. Baur, R. Bianchetti, J. M. Fink, M. Göppl, L. Steffen, and A. Wallraff, Using sideband transitions for two-qubit operations in superconducting circuits, *Phys. Rev. B* **79**, 180511(R) (2009).
- [84] S. A. Caldwell, N. Didier, C. A. Ryan, E. A. Sete, A. Hudson, P. Karalekas, R. Manenti, M. P. da Silva, R. Sinclair, E. Acala, *et al.*, Parametrically Activated Entangling Gates Using Transmon Qubits, *Phys. Rev. Applied* **10**, 034050 (2018).
- [85] M. Pechal, G. Salis, M. Ganzhorn, D. J. Egger, M. Werninghaus, and S. Filipp, Characterization and tomography of a hidden qubit, *arXiv:2011.08987*.
- [86] M. Jerger, A. Kulikov, Z. Vasselin, and A. Fedorov, *In Situ* Characterization of Qubit Control Lines: A Qubit as a Vector Network Analyzer, *Phys. Rev. Lett.* **123**, 150501 (2019).
- [87] M. A. Rol, L. Ciorciar, F. K. Malinowski, B. M. Tarasinski, R. E. Sagastizabal, C. C. Bultink, Y. Salathe, N. Haandbaek, J. Sedivy, and L. DiCarlo, Time-domain characterization and correction of on-chip distortion of control pulses in a quantum processor, *Appl. Phys. Lett.* **116**, 054001 (2020).
- [88] B. Foxen, J. Y. Mutus, E. Lucero, E. Jeffrey, D. Sank, R. Barends, K. Arya, B. Burkett, Y. Chen, Z. Chen, B. Chiaro, A. Dunsworth, A. Fowler, C. Gidney, M. Giustina *et al.*, High speed flux sampling for tunable superconducting qubits with an embedded cryogenic transducer, *Supercond. Sci. Technol.* **21**, 015012 (2019).